

This is to certify that the

thesis entitled

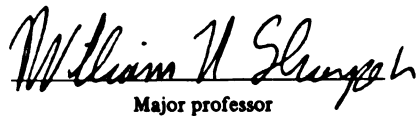
MEASUREMENT OF TRANSIENT RESPONSE
OF A
CENTRAL CRACK TO A TENSILE PULSE

presented by

Abdurahman Ahmed Sukere

has been accepted towards fulfillment
of the requirements for

Ph. D. degree in Mechanics


Major professor

Date July 29, 1979



OVERDUE FINES:

25¢ per day per item

RETURNING LIBRARY MATERIALS:

Place in book return to remove
charge from circulation records

--	--

MEASUREMENT OF TRANSIENT RESPONSE
OF A
CENTRAL CRACK TO A TENSILE PULSE

By

Abdurahman Ahmed Sukere

A DISSERTATION

Submitted to
Michigan State University
in partial fulfillment of the requirements
for the degree of

DOCTOR OF PHILOSOPHY

Department of Metallurgy, Mechanics and
Materials Science

1979

ABSTRACT

MEASUREMENT OF TRANSIENT RESPONSE OF A CENTRAL CRACK TO A TENSILE PULSE

By

Abdurahman Ahmed Sukere

The goal of this investigation was to study the behavior of a crack in a stress wave environment. The crack was approximated by electromachined slots in the center of thin aluminum specimens. A tensile impact apparatus has been developed for generating a plane tensile pulse with a ramp function profile. The amplitude and rise-time of the pulse were fairly repeatable. Dynamic displacements along the crack surface were measured using a laser interferometric displacement gage. The data were analyzed within the bounds of linear elastic fracture mechanics to estimate the dynamic stress intensity factor. The experimental results for the dynamic crack displacements were found to oscillate, a phenomena attributed to the cancellation and reinforcement of the incident waves by the various scattered waves. Analytical and numerical solutions compare favorably with the short time experimental results; i.e., with results for a time regime corresponding to the time it takes for the first scattered

Abdurahman Ahmed Sukere

P wave to travel from a crack tip to the nearest boundary and back. The comparison of the long time finite element solution with experimental is not good. The discrepancy may be attributed to the imperfect experimental wave front, the influence of which could not be isolated for this time regime.

ACKNOWLEDGEMENTS

I wish to extend a sincere thanks to Professor W.N. Sharpe, Jr., for his guidance and patience throughout the research program and for the experience and motivation provided by his research investigations. To Professor M.A. Medick, my gratitude for his encouragement and suggestions. Sincere thanks are also due to the other members of my guidance committee, Professor G.E. Mase and Professor L.J. Segerlind.

I would also like to thank Mr. D. Childs and Mr. R. Jenkins for assistance in constructing the apparatus.

TABLE OF CONTENTS

Chapter		Page
I.	INTRODUCTION	1
II.	EXPERIMENTAL TECHNIQUES	10
2.1	TENSILE PULSE GENERATING SYSTEM AND INSTRUMENTATION	10
	A. Background	10
	B. General Description and Principle of Operation	12
	C. Tensile Impact Apparatus	14
	D. Loading Machine	21
	E. Strain Pulse Measuring and Recording System	23
2.2	SPECIMEN GEOMETRY AND PREPARATION	28
	A. Material Properties	28
	B. Specimen Geometry	30
	C. Specimen Preparation	30
2.3	DISPLACEMENT MEASUREMENT	32
	A. Basics of the Interferometric Displacement Gate	32
	B. The IDG for Dynamic Displacement	37
	C. Relationship Between Displacement and Stress Intensity Factor	40
	D. Displacement Measuring and Recording System	43
2.4	PROCEDURES	44
	A. Preliminary Checks	44
	B. Eccentricity of Loading	49
	C. Testing Procedure	50

	Page
III. ANALYSIS OF CRACK RESPONSE TO LONGITUDINAL PLANE WAVES OF NORMAL INCIDENCE	53
3.1 ANALYTICAL CONSIDERATIONS	53
A. Equations of Elasticity in Two Dimensions	53
B. Formulation of the Problem	58
C. Solution of the Problem	61
3.2 EXPERIMENTAL DATA CONSIDERATIONS	65
A. Strain Time History of the Incident Wave	65
B. Dynamic Separation of Crack Faces	66
C. Dynamic Stress Intensity Factor	68
D. Dynamic Crack Profile	73
IV. RESULTS AND COMPARISON WITH THEORY	75
4.1 EXPERIMENTAL RECORDS	75
4.2 GENERAL CRACK BEHAVIOR	82
4.3 CORRELATION WITH ANALYSIS	93
4.4 COMPARISON WITH FINITE ELEMENT	96
V. SUMMARY AND CONCLUSIONS	102
LIST OF REFERENCES	105

LIST OF FIGURES

Figure		Page
2.1	Schematic of the experimental setup	15
2.2	Schematic of the tensile impact apparatus	16
2.3	Tensile pulse generating system	17
2.4	Close-up of projectile and tup assemblies	19
2.5	Schematic of hyge shock tester	22
2.6	Strain gage potentiometer circuit	24
2.7	Stress-strain of type 2219 aluminum	29
2.8	Schematic of the specimens	31
2.9	Schematic of the IDG	33
2.10	General view of the experimental setup	38
2.11	Photograph of the displacement measuring instrument	39
2.12	Notations used in measuring crack profile	41
2.13	Strain signal trigger circuit	45
2.14	Strain gage locations on the specimen before and after machining the slot	47
2.15	Observed strain response at various locations of the specimen without the slot	48
3.1	Geometry for generalized plane stress	54
3.2	Geometry of the problem	59
3.3	Experimental records for crack displacement at X_1 ($a/b = 0.54$)	67
3.4	Results of crack tip opening displacement for the trimmed specimen showing the displacement associated with each fringe pattern	69

Figure		Page
3.5	Local rectangular stress components	70
4.1	Experimental records for crack displacement at X_3 ($a/b = 0.167$)	76
4.2	Experimental records for crack displacement at X_2 ($a/b = 0.167$)	77
4.3	Experimental records for crack displacement at X_1 ($a/b = 0.167$)	78
4.4	Variations of displacement at X_3 with time for specimen with $a/b = 0.167$	83
4.5	Variations of displacement at X_2 with time for specimen with $a/b = 0.167$	84
4.6	Variations of displacement at X_1 with time for specimen with $a/b = 0.167$	85
4.7	Variation of dynamic stress intensity factor with time for specimen with $a/b = 0.167$	87
4.8	Variations of dynamic stress intensity factor with time for specimen with $a/b = 0.54$	90
4.9	Crack profile at three different time steps	91
4.10	Comparison of experimental dynamic k-calibration data with theoretical static results	92
4.11	Input pulse at location 2; experimental points and ramp function approximation	94
4.12	Comparison of analytical and experimental results for the dimensionless mode I stress intensity factor	95
4.13	Finite element model	98
4.14	Comparison of finite element and experimental results for the dimensionless mode I stress intensity factor	99

Figure		Page
4.15	Comparison of finite element and experimental results for the normalized displacement at the center	100

CHAPTER I
INTRODUCTION

Since the time of Griffith's [1] original idea (1920) that fracture of a brittle material is the result of the growth of inherent minute cracks or flaws, a series of technological problems of broad public interest has stimulated interest in the field of fracture mechanics. The U.S. Liberty ship episodes from 1940 to 1945 provide a vivid example. During that period more than 250 serious failures to ship hulls occurred due to factors associated with brittle fracture. These problems led to the modification of the Griffith idea, extension of the idea to metals and fatigue fracture, and the introduction of the concept of a critical stress intensity factor as a criterion for crack growth.

Research in this area has been greatly accelerated, resulting in a profusion of publications. This is because of fracture mechanic's past successes, ever increasing demand and because of the support and impetus provided by various governmental and industrial agencies.

For the most part, the physical systems which have been studied are quasi-static. In view of the fact that structures such as pipe lines, gun barrels, submarine hulls

and reactor components are subjected to dynamic loads that may be tensile in nature before or after reflection from interfaces, there are many fracture problems which cannot be viewed as being quasi-static and for which the inertia of the material must be taken into account. However, there are relatively few solutions available for the stresses in a cracked elastic solid subjected to dynamic loading. The primary reason for this is the extreme complexity of elastodynamic crack problems.

A comprehensive review of the literature regarding application of elastodynamics to the determination of stress intensities and to brittle fracture will not be undertaken here. In fact several very good and complete reviews have become available recently, among them those of Erdogan [2], Achenbach [3], [4], Sih [5] and Freund [6]. For the purpose of pertinence to the present work the literature concerned here relates to the class of elastodynamic problems that deals with a stationary crack subjected to time-dependent loads. The brief discussion that follows, also excludes solutions of idealized problems of cracks subjected to vertical shear (SV waves) waves and horizontal shear (SH waves) waves.

The stationary crack solutions which have been obtained can be put in one of two categories, depending on whether the applied load is periodic or transient. In the former category, significant progress has been made by Sih

and Loeber [7], who obtained effective solutions involving the interaction of wave length with crack size. Among the solutions of the latter category are the analysis of the scattering phenomenon of plane waves due to the presence of a semi-infinite crack by de Hoop [8], and Nuismer and Achenbach [9].

Mue [10], and Ang [11] explored transient problems in which a semi-infinite crack appears instantaneously in a uniformly stressed elastic medium. Their work was later extended by Baker [12], to the case where the crack propagates at a constant velocity after it has suddenly appeared. Equivalent problems have also been studied by Broberg [13] and Freund [14]. It is well to note that the mathematical formulation of the problems stated in References [10, 11, 12] are equivalent to the specification of a uniform impact loading on the surfaces of the crack. Furthermore, the running crack solutions of References [9, 12] can be reduced to stationary crack solutions by considering the crack velocity to be zero.

Transient problems for a finite length crack were explored by Papadopoulos [15], Thau and Lu [16], Ravera, Embley and Sih [17], and Chen and Sih [18]. The study in Reference [15] is qualitative in nature in that attention is focused on the closure of crack surfaces rather than obtaining quantitative results which characterizes the elastic fields in the vicinity of the crack tip.

Of particular interest to the present study is the work of Thau and Lu [16]. Thau and Lu used the Wiener-Hopf method to study the diffraction of a plane dilational wave of arbitrary profile and arbitrary angle of incidence by a finite stationary line crack in an infinite medium. They derived explicit expressions for the normal dynamic stress intensity factor, $k_1(t)$, and shear dynamic stress intensity factor, $k_2(t)$. The numerical results reported, which are exact for two crack transit times, are however only for the case of an incident Heaviside step stress pulse. Presented also in their study is the time history of the separation of crack surfaces at various points along the crack. Among the notable findings is the dynamic overshoot in k_1 and k_2 of about 30 percent compared with static values for the same loading.

The finite dimensions of the cracked specimen have been taken into account numerically by Chen [19], who used the finite difference method and by Anderson, Aberson and King [20], Glazik [21] and Aoki, et al. [22], who used the finite element method. Again the stress pulse was of the step variety, and References [19] and [20] report a dynamic normal stress intensity factor, $k_1(t)$, which is close to three times the static counterpart.

A substantial number of experimental studies have been conducted to investigate fracture dynamics phenomena. The studies in this field can be classified into two

categories according to the quantity intended for measurement. One category deals with a phenomenological investigation where the measured quantities of interest are magnitudes of pulse causing fracture, locations and types of fracture, velocity of running cracks and pulses generated due to sudden fracture. The other is concerned with an elastodynamic analysis where the measured quantities pertain to the transient strain or stress field near the crack tip.

The earliest work on the phenomenological type of experimental analysis was carried out by J. Hopkinson [23]. Hopkinson measured the strength of steel wires when they were suddenly stretched by a falling weight. The next significant investigation was carried out by B. Hopkinson [24], who detonated an explosive charge in contact with a metal plate. In this work, B. Hopkinson demonstrated the effect of "spalling" or "scabbing," which occurs when the compressive pulse generated by the explosive is reflected at the opposite side as a tensile pulse. More recently a very extensive investigation of this nature was carried out by Rinehart and Peterson [25]. Detailed descriptions of these and similar investigations can be found in a recent survey by Kolsky and Rader [26]. Roberts and Wells [27], Schardin [28], and Clark and Irwin [29] measured crack velocities in various materials. Later Kolsky [30] measured pulses generated by a brittle fracture

for the cases of Hertzian, simple tensile and flexural fractures.

The existing experimental works on fracture dynamics which are based on elastodynamic analysis are very few. Most of these studies were carried out by the methods of dynamic photoelasticity. Among the early works reporting the transient stress field surrounding a propagating crack for a statically loaded specimen are References [31-33]. In a later work Bradley and Kobayashi [34] made a study to correlate stress intensity factor with crack velocity. In 1969 Sommer and Soltesz [35] determined the dynamic stress intensity factor for an edge crack in a plate of Araldite B subjected to wave motions generated by a travelling air shock wave. Later Smith and Knauss [36] determined the critical stress intensity factor resulting from a stress wave loading for edge cracked Homalite 100 plates. The dynamic loads were applied directly to the crack surfaces by electromagnetic means. More recently Costin, Duffy and Freund [37] determined the fracture toughness for round bar steel specimens with prefatigued circumferential notches loaded to failure by rapidly rising tensile pulses. The wave motions were generated by explosive detonations and the pulses had a rise time of 35 to 40 microseconds at the fracture site. In 1978 Theocaris and Katsmanis [38] examined the behavior of notched plexiglas specimens under stress pulses created from an air-gun impact. In that investigation, plexiglas

plates of dimensions 300 x 40 mm and thickness 4 mm, and sawn notches of width 0.2 mm, and varying length (4, 6 and 10 mm) were impacted at one end by a steel sphere of diameter 10 mm. Using the method of caustics with a high-speed Crazz-Schardin camera, they determined the stress intensity factor and crack velocity of a running crack. Furthermore they made an attempt to correlate stress intensity factor and crack velocity and crack velocity and normalized crack length. However to the author's knowledge at present there are no experimental publications dealing with the interaction of a tensile stress pulse with a central crack in a thin strip. Furthermore, the studies of References [37] and [38], which have close relevance with the present investigation, lack an accurate determination of the loading applied to the plates.

Thus, the objectives of the present study are:

1. To develop experimental techniques for accomplishing a quantitative study of the elastodynamic stress fields in the vicinity of a stationary crack tip. These include a technique to generate a plane longitudinal tensile stress pulse in a plate with reasonable dimensions and a technique to measure dynamic crack displacement.
2. For a finite plate with a central crack, to study some aspects of the interaction of a

step-like tensile stress pulse with a crack that has neighboring boundaries. These include the time history of the separation of crack surfaces and the dynamic normal stress intensity factor.

3. To evaluate existing theory.
4. To provide some basic experimental data which can be used to guide future theoretical work.

The practical significances are:

1. To help upgrade fracture mechanics considerations in the design of structures and machine components by accounting for dynamic effects.
2. To help better understand geological failures such as mining operations, earthquakes and the interaction of ground shocks with faults in the earth's lithosphere.

The experimental techniques developed for this investigation are discussed in Chapter II. The first section describes the tensile pulse generating system and the instrumentation. The specimen geometry and preparation are described in section two. Also discussed in this chapter are the basics of the interferometric displacement gage (IDG), relationship between crack displacement and stress intensity factor, and the procedures used in the experimental work.

In Chapter III the theory of the dynamic response of a central crack to a tensile pulse in a plate is reviewed.

The data reduction procedure is also discussed here. The analytical work is based upon a two dimensional theory of elasticity for the case of generalized plane stress. The mode I dynamic stress intensity factor and the dynamic separation of crack surfaces were computed by employing the Duhamel superposition integral in conjunction with short time results, for Heaviside step loading, obtained by Thau and Lu [16]. The experimental work which takes into account the influence of the boundaries neighboring the crack was carried out using the IDG technique.

The results for the dynamic crack behavior are discussed in Chapter IV. It is believed that the results presented herein are the first experimental data on the dynamic response of a central crack with neighboring boundaries.

Chapter V, which summarizes the findings of this investigation, concludes the thesis.

CHAPTER II
EXPERIMENTAL TECHNIQUES

2.1 TENSILE PULSE GENERATING SYSTEM AND INSTRUMENTATION

A. Background

Tensile impact tests have been performed by many investigators, most of the tests being performed to determine the effects of loading rate on such properties as yield strength, energy absorption, reduction in area and elongation. The earliest work in this field was performed by J. Hopkinson [23] and Mason [39], both of whom applied tensile stress pulses to wires by means of a falling tup. Ginns [40] used a spring mechanism type loading machine to apply a sudden load and attempted to measure the stress with a resistance-pressure gage. Brown and Vincent [41], developed a pendulum type impact machine and used piezoelectric crystals to measure stress. Clark [42], Mann [43] and Nadi and Manjoine [44] all used versions of a high speed rotary impact machine. The impact was applied by two hammers mounted on a heavy fly-wheel which was rotated by a variable speed direct current motor. At a predetermined speed the hammers were allowed, by means of a trigger mechanism, to engage an anvil fastened to the bottom of the specimen.

Clark and Wood in a paper of 1949 [45] described the construction of a new type of a tensile impact machine in which the load is applied pneumatically and reaches a maximum in times as short as 5 milliseconds. In 1959 Austin and Steidel [46] developed an explosive impact tensile tester.

All of the above-mentioned techniques suffered one or more of the following problems: distortion of the pulse due to vibration, non-axial loading and long rise time. The difficulty of axial loading may be adequately overcome, if care is taken, in tests involving compression impact, but when a tensile load has to be applied the problem is more difficult.

Various attempts have been made to reduce the effect of non-axial impact. One solution [47] has been to use a hollow cylindrical specimen fixed at one end and impacted at the other by a bullet which has travelled down its length. The requirement of a specialized design of specimen makes this technique undesirable. Harding et al. [48] developed an apparatus in which a tensile stress (strain) pulse was obtained by reflection of the loading wave which produced a compression impact on a tubular weighbar fastened to the top, so that the eccentricity of tensile loading is improved to that of a compression impact test. With this loading machine they were able to produce loading pulses as short as 25 microseconds which

could have been improved if the impact had been at the tup, since the travel in the weighbar contributes to the deterioration of the rise-time of the compression pulse.

Later on, Harding [49] developed a magnetic loading machine in which the tup was accelerated away from a coil when a capacitor bank was discharged through the coil. This produced loading pulses with rise-times as short as 5 microseconds. The main problem with this technique is the large transient electrical field associated with the discharge. He allowed the pulse to travel for 60 microseconds before it reached the specimen so that the transient would die out and resistance strain gages could be used.

More recently, 1977, Costin et al. [37] developed an explosive impact tensile tester which is an adaptation of the Klosky pressure bar. The tensile pulse was produced by detonating an explosive charge on a loading head attached to the end of the bar by a large bolt. Reflection of the compressional wave from the back face of the loading head produced a tensile pulse in the bolt, which was transmitted to the end of the bar. The rise time measured at the incident gage was 20 to 25 microseconds and that at the site of interest was 35 to 40 microseconds.

B. General Description and Principle of Operation

Because the primary interest of the present investigation was the response of the impingement of plane

stress waves on a crack, it was necessary to devise an apparatus that would generate plane waves over a relatively large area representing one edge of the specimens.

As noted in the preceding section the tensile pulse generating devices used to date are designed for round bar specimens, which makes the problem of non-axial impact relatively easy. Thus it became apparent that the strain-wave generation devices currently in use were either unsuitable or too expensive a venture to adapt for this investigation. It was then decided to design and construct a new type of a tensile impact apparatus that would satisfy the following criteria:

- 1) Capable of generating plane tensile stress waves that resemble a Heaviside step function, to facilitate comparison with theory.
- 2) Capable of allowing the input pulse to reach its maximum before reflected waves from the boundary of reasonable size specimens reach the crack, i.e. the rise-time of the pulse should be on the order of 10 microseconds or less.
- 3) Capable of producing repeatable pulses.
- 4) Should have provisions that would enable the amplitude of the pulse to be varied.
- 5) Should have provisions to make specimens accessible for optical measurement.

- 6) Should be inexpensive to build, and
- 7) Should be easy to operate.

The major components of the pulse generating system were the loading machine and the tensile impact apparatus. A schematic representation is shown in Figure 2.1. The loading machine has an attached loading assembly that accelerates a projectile which rides down a launch tube and impacts a tup. During contact, compression waves travel away from the impacting interface in both the projectile and the tup. Meanwhile, a tensile wave travels through the specimen away from the tup. Since the projectile is shorter in length in comparison with the tup, when the wave reflected (as tensile) from the end of the projectile reaches the interface, the projectile is thrown back. Thus, the length of the projectile determines the duration of the "square" pulse. Brass was chosen for the material of the impactor and the tup on account of its low stress wave velocity, and their respective length dimensions were chosen to give the necessary pulse duration. A detailed discussion of the construction of apparatus is given in the following two sections.

C. Tensile Impact Apparatus

The arrangement and dimensions of the tensile impact apparatus are shown in Figures 2.2, 2.3, and 2.4. The apparatus consisted of four main components; a launch tube, a loading assembly, a projectile assembly and a tup.

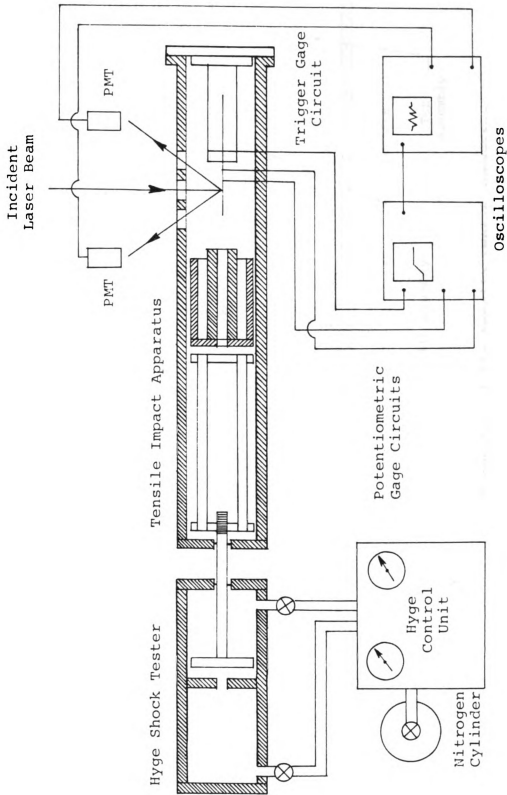


Figure 2.1. Schematic of the experimental setup.

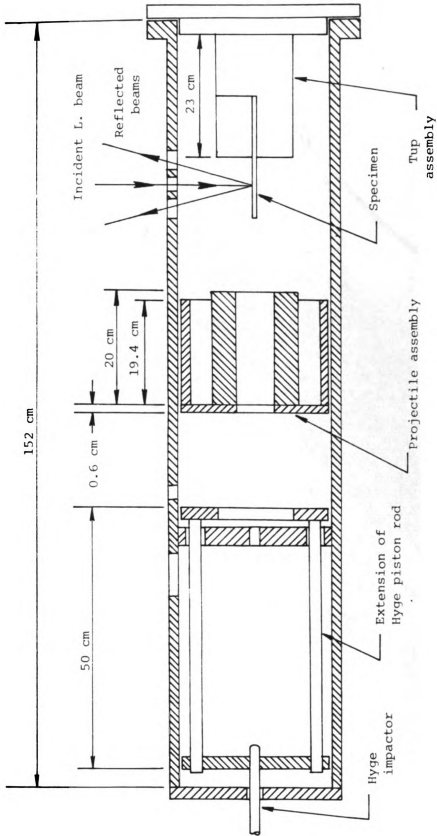


Figure 2.2. Schematic of the tensile impact apparatus.

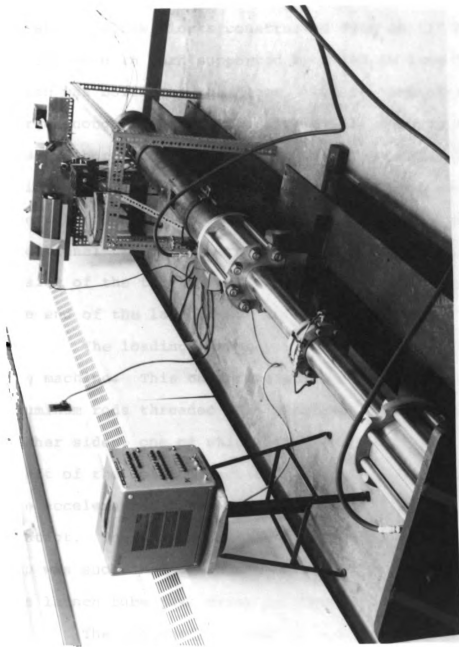


Figure 2.3. Tensile pulse generating system.

The launch tube was a commercially available cold-drawn seamless steel tube with an inner diameter of 15.240 ± 0.058 cm, an outer diameter of 17.78 cm and a length of 152 cm. This launch tube was supported securely in steel pillow blocks constructed from an "I" beam. The blocks were in turn supported by a 183 cm long "I" beam which was bolted to the floor. Due to lack of a lathe large enough to handle the size of the tube no attempt was made to bore it for a more precise clearance. Three ports, which were later fitted with quartz windows, were cut in the tube to allow optical measurements on the specimen. Additional two ports were cut in to allow access to the inside of the tube. Furthermore, a collar was welded on one end of the launch tube to attach the tup.

The loading assembly is an extension of the loading machine. This unit consists of two parallel aluminum rods threaded onto aluminum circular plates on either sides, one of which was threaded onto the piston shaft of the loading machine, the other left free to apply the accelerating force on the projectile assembly when in contact. The spacing between the loading assembly and the tup was such that the projectile was in free motion within the launch tube just prior to impact.

The projectile assembly (see Figure 2.4), which was supported within the bore of the launch tube, consisted of a rectangular C shaped brass impactor, a

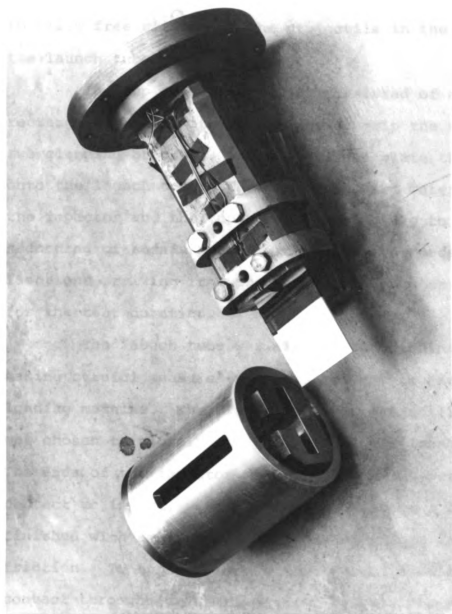


Figure 2.4. Close-up of projectile and tup assemblies.

cylindrical aluminum supporting and guiding structure, and a steel end plate which held the impactor and the cylinder together. The impactor and the supporting cylindrical structure were designed with provisions to allow optical measurement on the specimen. Some lubrication was applied to allow free sliding of the projectile in the bore of the launch tube.

The tup (see Figure 2.4) consisted of a two piece rectangular brass with serrations to grip the specimen, two clamping brackets, and a steel end plate that bolts onto the launch tube. The dimensions and materials of the impactor and the tup were chosen partly to permit the recording of strain pulses without interference from reflections arriving from the ends of the tup or impactor for the test duration.

The launch tube was aligned longitudinally by making careful measurements with respect to parts of the loading machine. The diameter of the projectile assembly was chosen to closely fit the bore of the launch tube. The ends of the impactor and the tup, which were to be in contact at impact, were carefully turned in a lathe and finished with emery paper in order to reduce lateral friction. To further assure substantial simultaneity of contact throughout the surface of contact there was the provision for inserting shims between the brass bar and the end of plate of the tup.

D. Loading Machine

The projectile assembly was accelerated by means of a commercial Hyge Shock Tester, Type HY-3422, manufactured by Consolidated Electrodynamics Corporation. The tester is shown in Figure 2.3 and a schematic is shown in Figure 2.5. The piston diameter is 7.62 cm and the full stroke is 42.55 cm.

The acceleration of the piston is achieved in the following manner: A given set pressure is applied to chamber B by means of compressed nitrogen. This pressure acts over the full area of the piston, pushing it against a ring seal at C. A load pressure is then applied to chamber A, this pressure being restricted to a smaller area of the piston by the ring seal thus causing a smaller force to act on this side of the piston. When the load pressure reaches a magnitude of 4.2 times that of the set pressure, the forces acting on the piston become equal. If additional load pressure is applied, the seal at C is broken and the load pressure expands over the entire face of the piston causing a large acceleration.

The acceleration is regulated by a conical pin which regulates the amount of gas supplied to the piston face during the initial part of the acceleration. The acceleration is aided by a hydraulic fluid which occupies approximately one-half of the volume of chamber B. The deceleration is accomplished by a pin which gradually

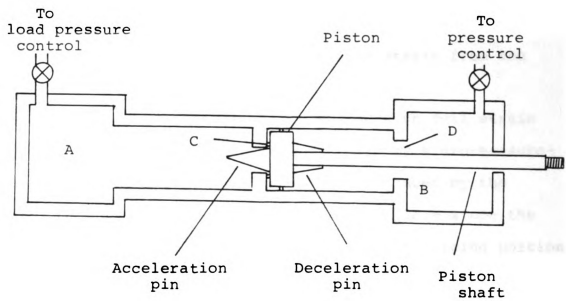


Figure 2.5. Schematic of Hye Shock Tester.

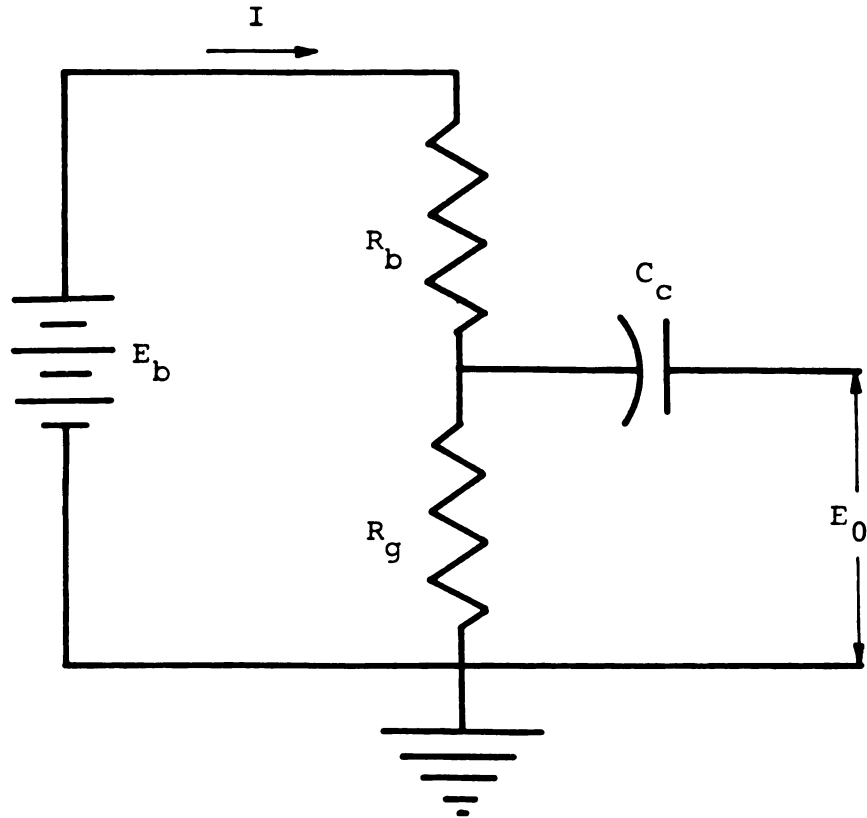
closes the area of the escape orifice D through which the hydraulic fluid is forced. The system is controlled from a separate control panel which contains pressure gages and control valves.

E. Strain Pulse Measuring and Recording System

Resistance strain gages change resistance when they are subjected to a strain. A potentiometer circuit converted the resistance change into a voltage change. Calibration factors then determined the strain from the voltage change.

The specimens were instrumented with foil strain gages type ED-DY-062AA-350, manufactured by Micro-Measurements. The distortion of the pulse introduced by the 0.157 cm gage length was considered negligible since the gage length was small in comparison with the rising portion of the pulse. The resistance of this gage as given by the manufacturer was 350 ohms \pm 0.4 percent and the gage factor was 3.16 \pm 2.0 percent. The circuit voltage was supplied by a six volt battery, and the voltage was recorded before each test by means of a voltmeter connected in parallel with the battery.

The potentiometer circuit is shown in Figure 2.6. A ballast resistor, R_b , is in series with the strain gage, R_g . For any fixed supply voltage, E_b , the maximum sensitivity of the circuit will occur when $R_b = R_g$. The coupling capacitor, C_c , prevents the passage of direct current to



E_b : Circuit supply voltage (DC)

I : Circuit current

R_b : Ballast resistor

R_g : Strain gage

C_c : Coupling capacitor

E_0 : Output voltage

Figure 2.6. Strain gage potentiometer circuit.

the recording instrument. Thus, this circuit will only respond to dynamic strains or the dynamic components of combined strains.

By Ohm's Law the current in the circuit is

$$I = E_b / (R_b + R_g) \quad (2.1)$$

and the voltage across the gage is

$$E_g = I R_g \quad (2.2)$$

Substituting Equation (2.1) into Equation (2.2), gives the voltage across the strain gage as

$$E_g = E_b R_g / (R_b + R_g)$$

Applying a strain to the gage changes the gage resistance to $R_g + \Delta R_g$.

The current then becomes

$$I = E_b / (R_b + R_g + \Delta R_g) \quad (2.3)$$

and the voltage across the gage becomes

$$E_g + \Delta E_g = I (R_g + \Delta R_g) \quad (2.4)$$

Substituting Equation (2.3) into Equation (2.4) gives the new voltage across the gage as

$$E_g + \Delta E_g = \frac{E_b (R_g + \Delta R_g)}{(R_b + R_g + \Delta R_g)} \quad (2.5)$$

Successive algebraic operations on Equation (2.5) give

$$\begin{aligned}
E_g + \Delta E_g &= E_b R_g (1 + \Delta R_g / R_g) / \{ (R_b + R_g) [1 + R_g / (R_b + R_g)] \} \\
&= \frac{E_b R_g (1 + \Delta R_g / R_g)}{(R_b + R_g)} [1 - (\Delta R_g / (R_b + R_g)) \\
&\quad + (\Delta R_g / (R_b + R_g))^2 - (\Delta R_g / (R_b + R_g))^2 + \dots] \\
&= \frac{E_b R_g}{R_b R_g} [1 + \Delta R_g R_b / R_g (R_b + R_g) - \Delta R_g^2 R_b / R_g (R_b + R_g)^2 \\
&\quad + \Delta R_g^3 R_b / R_g (R_b + R_g)^3 - \dots] \quad (2.6)
\end{aligned}$$

The first term on the right hand side of Equation (2.6) is E_g which is the DC component of the voltage across R_g . The remaining terms are then the dynamic component of the voltage across the gage. Since the coupling capacitor will only pass the dynamic component of the voltage, we have as a circuit voltage

$$E_0 = \Delta E_g \quad (2.7)$$

Thus Equations (2.6) and (2.7) give

$$\begin{aligned}
E_0 &= \frac{E_b R_b R_g}{(R_b + R_g)^2} [1 - \Delta R_g / (R_b + R_g) \\
&\quad + R_g^2 / (R_b + R_g)^2 - \dots] \quad (2.8)
\end{aligned}$$

Typical foil strain gages subjected to elastic strains have the following values:

$$R_g = 120 \text{ or } 350$$

$$\Delta R_g < 2\Omega$$

Therefore, the higher order terms in Equation (2.8) can be neglected; this results in an error in E_0 of less than one percent. The output voltage for foil gages is then

$$E_0 = \frac{E_b R_b \Delta R_b}{(R_b + R_g)^2} \quad (2.9)$$

Two Tektronix preamplifiers were used to amplify the signals from the potentiometric circuits. Tektronix Type 1A7A plug-in preamplifier was used for the upper trace signal. This is a high gain differential preamplifier with a vertical sensitivity to 10 microvolts per centimeter and a frequency response from DC to 1 megahertz.

The lower trace signal was amplified with the use of a Tektronix Type 1A1 dual-trace plug-in preamplifier. Both channels of the Tektronix Type 1A1 plug-in-unit had a vertical sensitivity to .005 volts per centimeter. In order to pick up the low-level strain signals Channel 1 was used as a wide band AC-coupled 10X preamplifier for Channel 2 by connecting Channel 1 and Channel 2 in cascade with coaxial cable meant for this purpose. The resulting output noise level was reduced by inserting a low-pass filter between the Channel 1 signal output and the Channel 2 input.

The preamplifiers were mounted in a Tektronix Type 551 dual beam oscilloscope which permitted the signals from two gage stations to be displayed at the same time with one horizontal sweep of the beams. The sweep speed

could be varied from 0.1 microsecond per centimeter to five seconds per centimeter. The input impedance of the oscilloscope was one $M\Omega$. This value was much greater than the strain gage resistance. Therefore, the effect of the oscilloscope impedance on the output of the potentiometer circuit was negligible. The scope was triggered by means of a delayed trigger signal from the Tektronix Type 555 oscilloscope.

A record of the oscilloscope trace was obtained by using a Tektronix camera system type C-12 with Polaroid Land film type 47. Using an open shutter at a setting of $f1.9$ and an oscilloscope sweep speed of 5 microseconds/centimeter a clear picture of each trace was recorded.

2.2 SPECIMEN GEOMETRY AND PREPARATION

A. Material Properties

The specimen material was Type 2219 aluminum 1/8 inch (3.2 mm) thick furnished by NASA-Lewis. The specimen was oriented so that the rolling direction was parallel to the loading direction. The stress-strain curve from an ASTM specimen with the same orientation is shown in Figure 2.7. This curve was obtained using an Instron test machine and foil gages on the specimen. Another specimen was instrumented with foil gages in the longitudinal and transverse directions to obtain Poisson's Ratio. From these data, the elastic properties are determined to be:

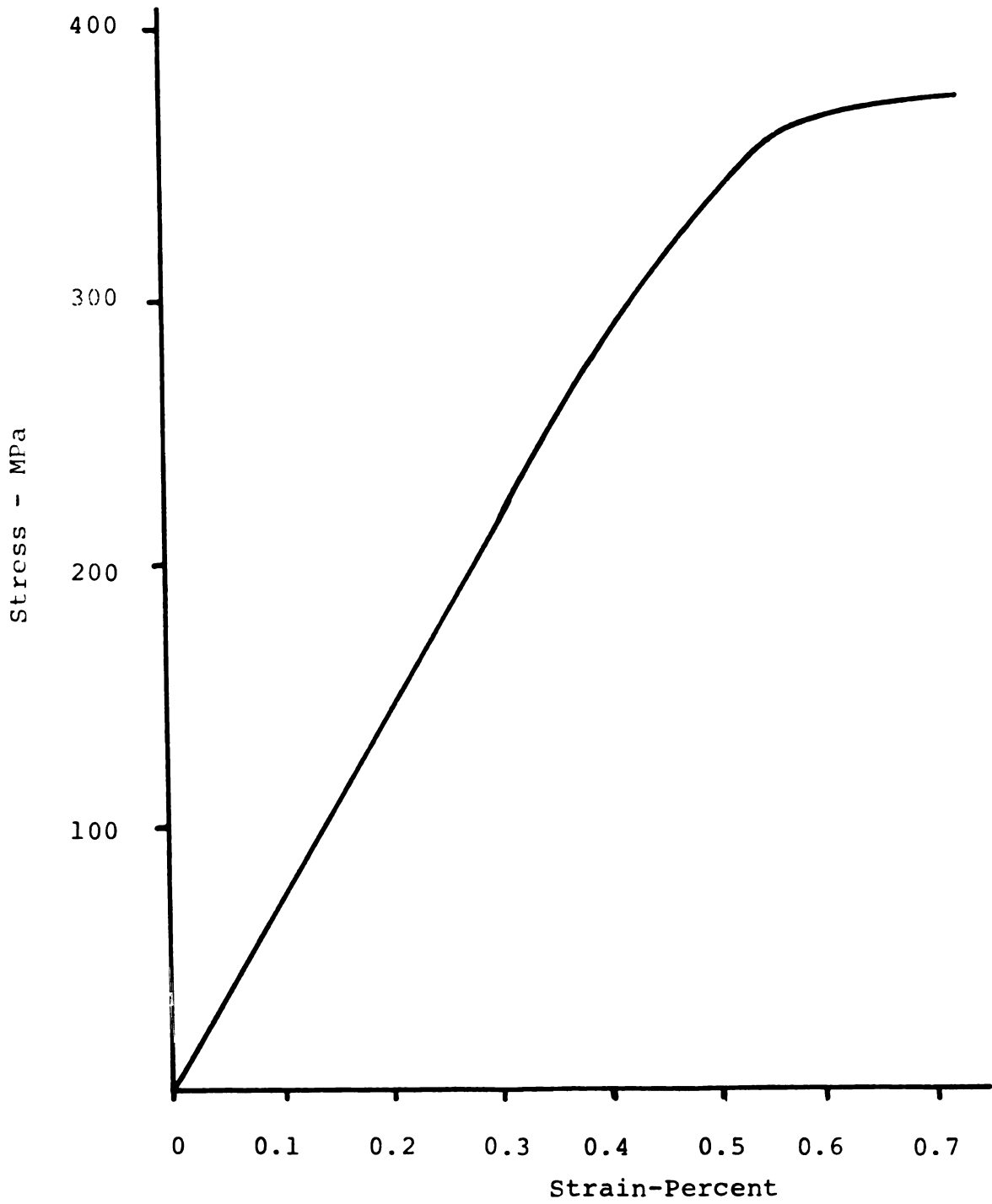


Figure 2.7. Stress-strain of type 2219 aluminum.

$$\text{Elastic Modulus} = 70 \pm 1 \text{G Pa}$$

$$\text{Poisson's Ratio} = 0.33 \pm 0.01$$

B. Specimen Geometry

A schematic of the specimen is given in Figure 2.8. The dimensions of the plate specimen were determined by three considerations. The maximum thickness was governed by the desire to reduce geometric dispersion to negligible proportions for the frequencies contained in the stress pulse. The lateral dimensions are chosen to produce reasonable levels of strain relative to electrical noise and to yield an essentially plane wave front for this type of excitation away from the impact point. Furthermore, the intention to compare results with previous static measurements of crack behaviors forced the selection of specimen with dimensions 0.32 cm x 7.62 cm x 20.32 cm.

C. Specimen Preparation

A slot nominally 12.5 mm long was electromachined in the plate specimen. The thickness of the slot was measured at five positions along the slot - at the ends (x_1 and x_5), the middle (x_3) and the quarter-points (x_2 - x_4) as indicated in Figure 2.8. The data on the slot geometry are measured to be

$$t|_{x_1} = .314 \text{ mm}, t|_{x_2} = .307 \text{ mm}, t|_{x_3} = .313 \text{ mm},$$

$$t|_{x_4} = .290 \text{ mm}, t|_{x_5} = .320 \text{ mm}$$

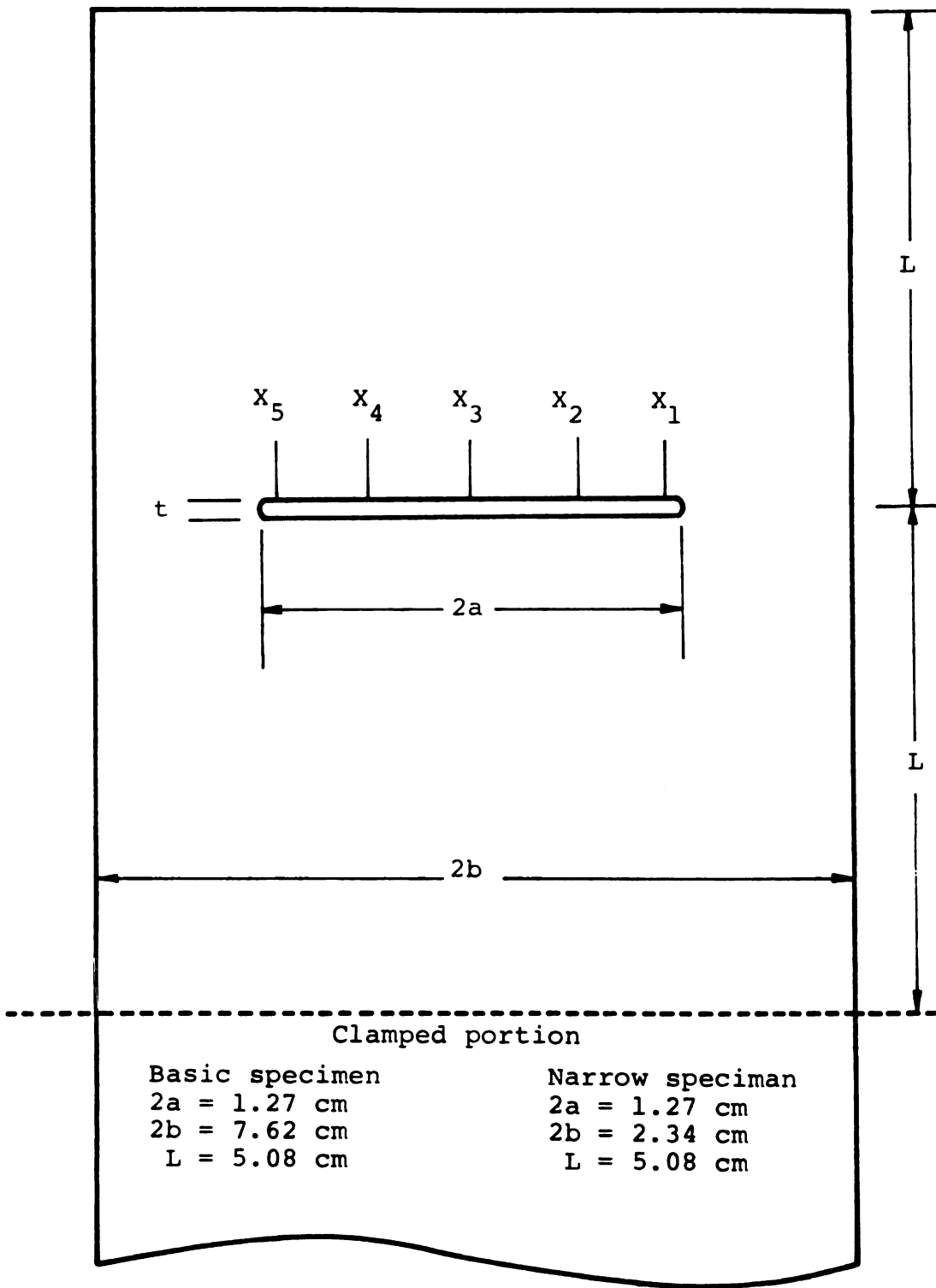


Figure 2.8. Schematic of the specimens.

The preparation and maintenance of the specimen surface is critical for generating useable fringe patterns since the patterns are degraded by stray reflections surrounding the indentations. A flat surface was attained on the specimen by first sanding with 320, 400, and 600 grit metallurgical paper and then polished with 1 micron and finally 0.3 micron alumina paste following standard metallurgical procedures.

The reflective indentations were applied to the specimen surface with a Vicker's hardness tester using the 100 p weight. The crosshairs in the x-y micrometer stage of the microhardness tester allow placement of the indentation in the desired locations to within ± 2 microns if care is taken.

2.3 DISPLACEMENT MEASUREMENT

A. Basics of the Interferometric Displacement Gages

Shallow reflective indentations are pressed into the polished surface of the specimen on either side of a crack or slot as shown in Figure 2.9. When coherent light impinges upon the indentations, it is diffracted back at an angle (α_0) with respect to the incident beam shown schematically in Figure 2.9. Since the indentations are placed close together, the respective diffracted beams overlap, resulting in interference fringe patterns on either side of the incident laser beam.

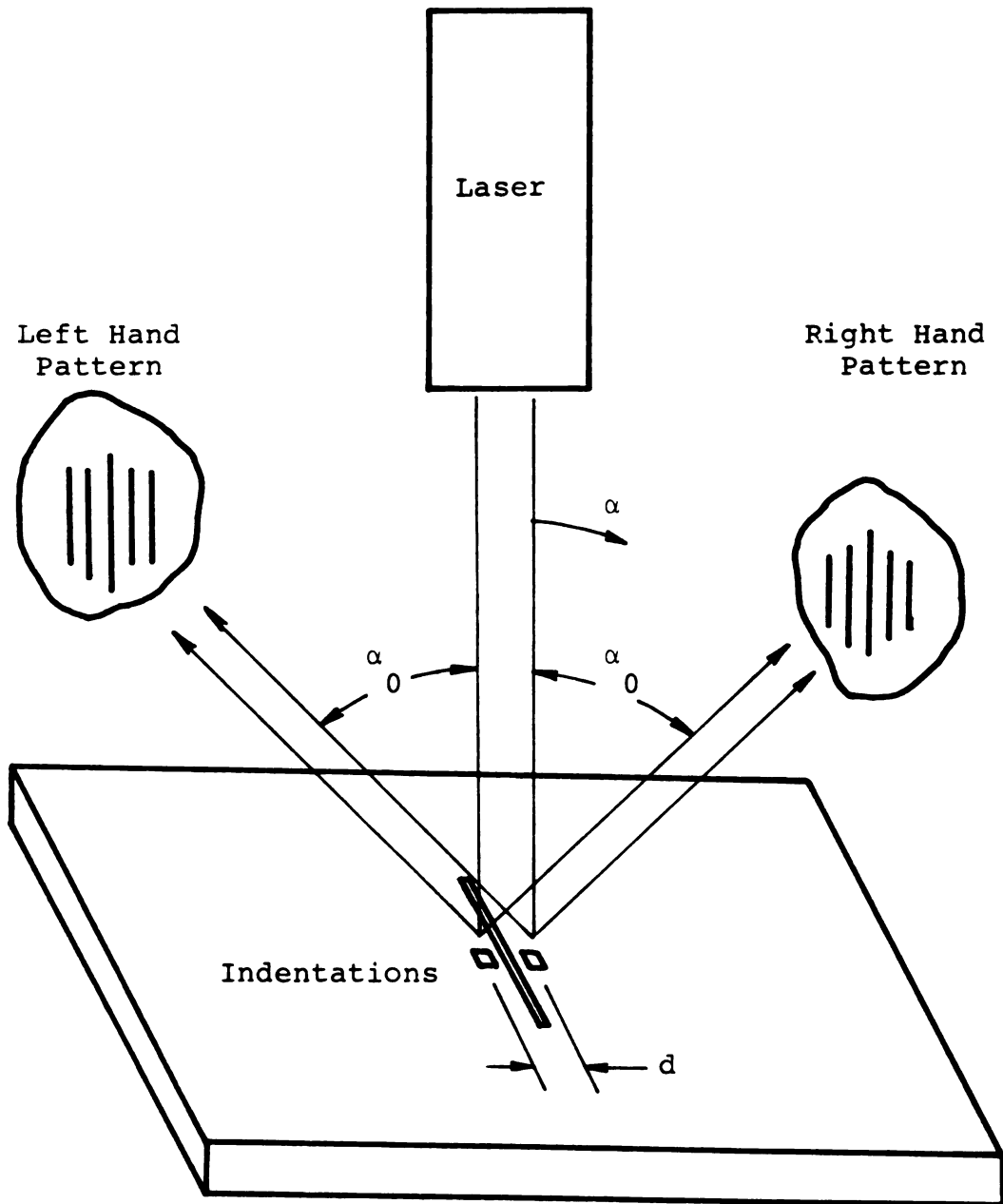


Figure 2.9. Schematic of the IDG.

In observing the fringe pattern from a fixed position at the angle α_0 , fringe movement occurs as the distance (d) between the indentations changes. Application of a tensile load, causing the distance between the indentations to increase, results in positive fringe motion towards the incident beam. Conversely, the removal of the tensile load results in negative fringe motion away from the incident beam.

The intensity, I, of the fringe pattern is given by [50], [51]

$$I = I_0 \frac{\sin^2 \beta}{\beta^2} \cos^2 \xi \quad (2.10)$$

where

$$\beta = \frac{\pi W}{\lambda_0} (\sin \alpha_0 - \sin \alpha)$$

and

$$\xi = \frac{\pi d}{\lambda_0} \sin \sigma$$

In these equations, I_0 is the maximum intensity at the center of the pattern, W is the width of an indentation side, d is the spacing between indentations, λ_0 is the wave length of light, and α and α_0 are defined in Figure 2.9. In Equation (2.10) the $\cos^2 \xi$ term is modulated by the more slowly varying $\sin^2 \beta / \beta^2$ term since $W \ll d$.

If one now fixes the observation position at α_0 and monitors the intensity changes as d changes, Equation (2.10) becomes

$$I = I_0 \cos^2 \left(\frac{\pi d}{\lambda_0} \sin \alpha_0 \right) \quad (2.11)$$

The intensity has a minimum whenever

$$\frac{d}{\lambda_0} \sin \alpha_0 = (m + \frac{1}{2}), \quad m = 0, \underline{+1}, \underline{+2}, \underline{+3}, \dots$$

Using this as a basis one can then write the relationship between the indentation spacing and the fringe order shown schematically in Figure 2.7 as

$$d \sin \alpha_0 = m \lambda_0 \quad (2.12)$$

Here m is the fringe order, and α_0 the angle between the incident and reflected beams, thus defining the zeroth fringe order.

The relationship between the change of indentation spacing (δd) and the change in fringe order (δm) is given by

$$\delta d = \frac{\delta m \lambda_0}{\sin \alpha_0} \quad (2.13)$$

It is this relation that serves as the basis of the IDG.

Fringe motion can be caused by rigid body motion as well as relative displacements. When the specimen moves parallel to its surface and along a line between the indentations, one fringe pattern moves toward the incident beam, and one moves away. Therefore, averaging the fringe motions eliminates the rigid body motion, and one should calculate the displacement from:

$$\delta d = \frac{\lambda_0}{\sin \alpha_0} \left(\frac{\delta m_1 + \delta m_2}{2} \right) \quad (2.14)$$

This component of rigid-body motion is present in every ordinary system for loading specimens, so that it is very important that it be averaged out. Other rigid-body motions (e.g., one perpendicular to the specimen surface) are not averaged out and can lead to errors. In carefully aligned testing machine this components of rigid-body motion can be made small, eliminating the need for corrections.

Using typical values of $\lambda_0 = 0.6328$ microns (He-Ne laser) and $\alpha_0 = 42^\circ$, the calibration constant $\lambda_0/\sin \alpha_0$ is 0.95 microns. In other words, when one complete fringe shift has been observed, the corresponding displacement is about one micron.

The gage consists of two reflecting indentations. These are applied with a Viker's harness tester which, with its diamond indenter, permits the accurate application of high quality pyramidal indentations. These indentations are typically 25 microns long on each side and can be placed as close as 25 microns to the edge of a crack.

The sensitivity of the displacement measurement is determined by the quantity $\lambda_0/\sin \alpha_0$ in Equation (2.14) and by the capability of measuring fractions of a fringe shift. For large displacements the measuring of one-half of a fringe shift is sufficiently sensitive since this refers to a displacement half a micron.

A very small δm can be resolved if one has a record of the absolute intensity variation at a position on the pattern about one-half the distance between a maximum and minimum.

B. The IDG for Dynamic Displacement

The technique for dynamic interferometric displacement measurement described here is essentially similar to that used previously by Sharpe [52]. A schematic of the setup for the dynamic displacement measurement is given in Figure 2.1, and photographs are shown in Figures 2.10 and 2.11. Convenience of the arrangement necessitated the use of a mirror to direct the laser beam onto the indentations; it is important that this mirror not only has a high reflectivity but also be flat in order to preserve the coherence of the laser beam. A dielectric mirror with a reflectivity of 99.7 percent that is flat to 1/10 wavelength was used. The three point adjusting feature on the mirror guarantees the easy adjustment of the light field on the indentations.

With this technique one simply monitors the fringe shift of each pattern by a photomultiplier tube whose window is covered except for a thin slit with a width less than the width of a fringe in a pattern. As the fringes pass over this slit, the intensity seen by the photomultiplier tube varies and, in the ideal case, the output signal is a sine wave. Adjusting the fringe pattern so

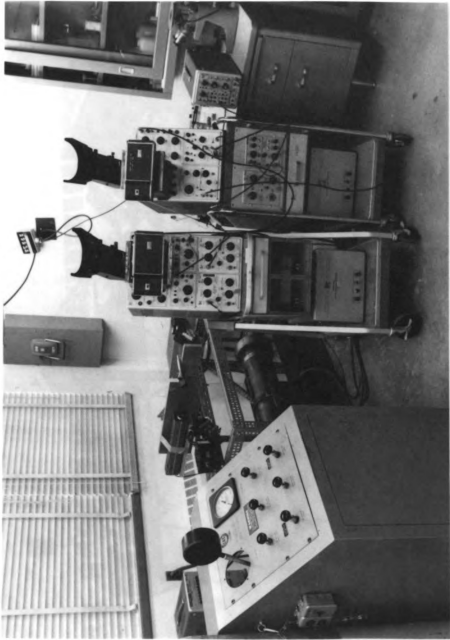


Figure 2.10. General view of the experimental setup.

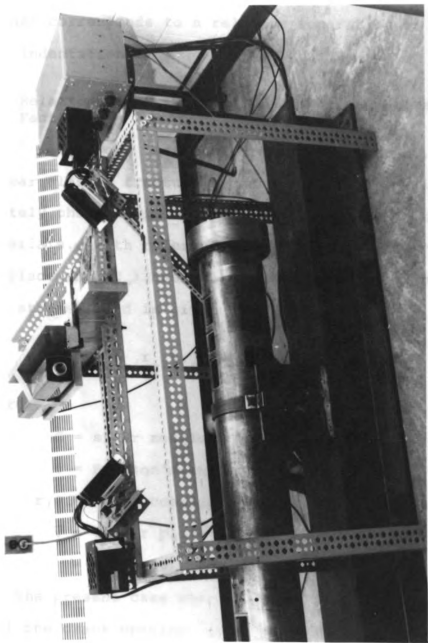


Figure 2.11. Photograph of the displacement measuring instrument.

that the static signal from the photomultiplier tube is midway between maximum and minimum and observing the position of the nearest bright or dark fringe relative to the slit, permits one to determine whether the displacement signal corresponds to a relative separation or closing of the indentations.

C. Relationship Between Displacement and Stress Intensity Factor

The mode I stress intensity factor, k_1 , is the linear elastic fracture mechanics parameter which adequately characterizes crack behavior near the tip in many materials. With reference to Figure 2.12 the y-direction displacement (U_y) associated with the opening mode crack tip stress field is given by [53]

$$U_y = \frac{k_1}{G} \left(\frac{r}{2\pi}\right)^{\frac{1}{2}} \sin \frac{\theta}{2} [2 - 2\bar{\nu} - \cos^2 \frac{\theta}{2}] \quad (2.15)$$

where

G = shear modulus

ν = Poisson's ratio

r, θ = Polar coordinates referred to the crack tip

$\bar{\nu} = \nu$, for plane strain

$= \nu/(1 + \nu)$ for plane stress

For the present case where plane stress conditions prevail the crack opening (U_x^0) near the tip may be given as

$$U_y^0 = \frac{2k_1}{G} \left(\frac{r}{2\pi}\right)^{\frac{1}{2}} \sin \frac{\theta}{2} \left[\frac{2}{1+\nu} - \cos^2 \frac{\theta}{2}\right] \quad (2.16)$$

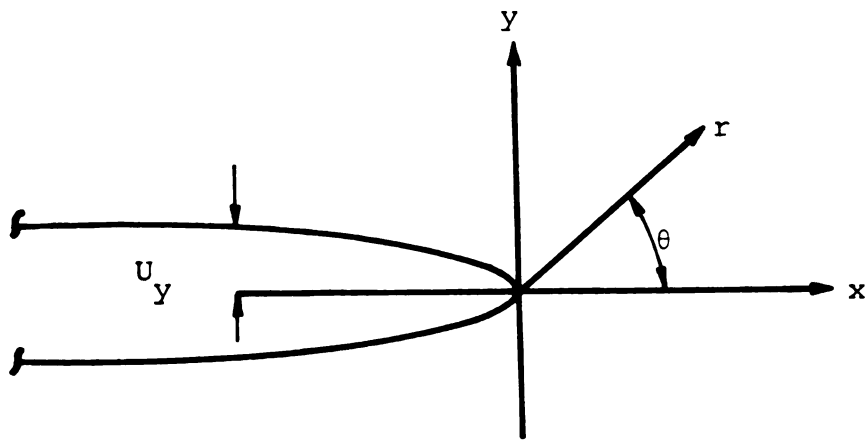


Figure 2.12. Notations used in measuring crack profile.

Examining Equation (2.16) it is obvious that with the knowledge of elastic constants G and ν , and careful measurements of r, θ , and the vertical separation of crack surfaces near the tip one can determine the mode I stress intensity factor. In fact, such measurements have been made with great success by many researchers.

Adams [54] used a photographic technique to measure the relative displacement of identifiable surface markings astride a fatigue crack and only 76 microns apart. His technique, though somewhat laborious, could be used to obtain k . Elber [55] developed an accurate clip gage with gage length of 1.27 mm that could be used for k -calibrations of larger specimens. Dudderar and Gorman [56] made k measurements in thin PMMA sheet specimens using holographic interferometry to measure the displacement perpendicular to the sheet. Their technique is applicable only to thin transparent models. Sommer [57] and Crosely et al. [58] measured the crack displacements inside glass models by optical interferometry and used them to determine k . The advantage of interior displacement measurements near the crack tip is offset by the transparency requirement of the specimen. Evans and Luxmore [59] used the laser speckle method to measure inplane displacements on the specimen surface. A brittle plastic specimen was used, but the technique works on metals as well. Sharpe and Grandt [60, 61], Macha, Sharpe and Grandt [62],

Sharpe [63], [64] used a laser interferometric technique to measure crack surface displacements. This technique which is adapted for the present research program can be used to measure displacements of 0.02 microns at 50 microns from the crack tip. Further details of the technique are given in section B.

The hitch to the measurement of the stress intensity factor is the requirement of a technique capable of measuring small displacements very near the crack tip. As a rule of thumb the displacement relations given in Equation (2.16) are regarded to be sufficiently accurate within a distance $a/10$ from the crack tip, where "a" is half the crack length [65].

D. Displacement Measuring and Recording System

The photomultiplier tubes used were Amperex Type XP-1117 with a divider circuit load resistance of 1k and an operating voltage of 1500V. The output from each photomultiplier tube was fed into a Tektronix Type 53/54 D plug-in preamplifier. These are high gain differential amplifiers with a vertical sensitivity of 1 mv and a frequency response from .35 to 2MC.

The two plug-in preamplifiers were mounted in a Tektronix Type 555 dual beam oscilloscope. The output from each photomultiplier tube was thus recorded simultaneously on separate channels of the oscilloscope. The sweep speed of the oscilloscope could be varied from

0.1 microseconds/cm to five seconds/cm. The sweep was triggered by a differentiated signal from a foil strain gage mounted on the tup about 0.64 cm from the impacting interface. A schematic of the triggering circuit is shown in Figure 2.13 [66].

A Tektronix Type 0 operational amplifier unit was used in the differentiator circuit. The unit consisted of three parts: a vertical preamplifier and two operational amplifiers. The vertical amplifier was such that it can be used either as an independent oscilloscope preamplifier or to monitor the output of either of the operational amplifiers. The operational amplifiers could be used for applications involving integration, differentiation as well as many others. Besides having provisions for selecting input and feedback impedances, C_i and R_f , from several values, the Type 0 unit had an internal circuitry to limit high frequency response.

A record of the oscilloscope trace was obtained by using a Tektronix camera system type C-12 with Polaroid Land film, type 47. Using an open shutter at a setting of f1.9 and an oscilloscope sweep rate of 5 microseconds/cm a clear picture of each trace was recorded.

2.4 PROCEDURES

A. Preliminary Checks

In order to check the applicability of the plane stress assumption, we can consider simple normal impact

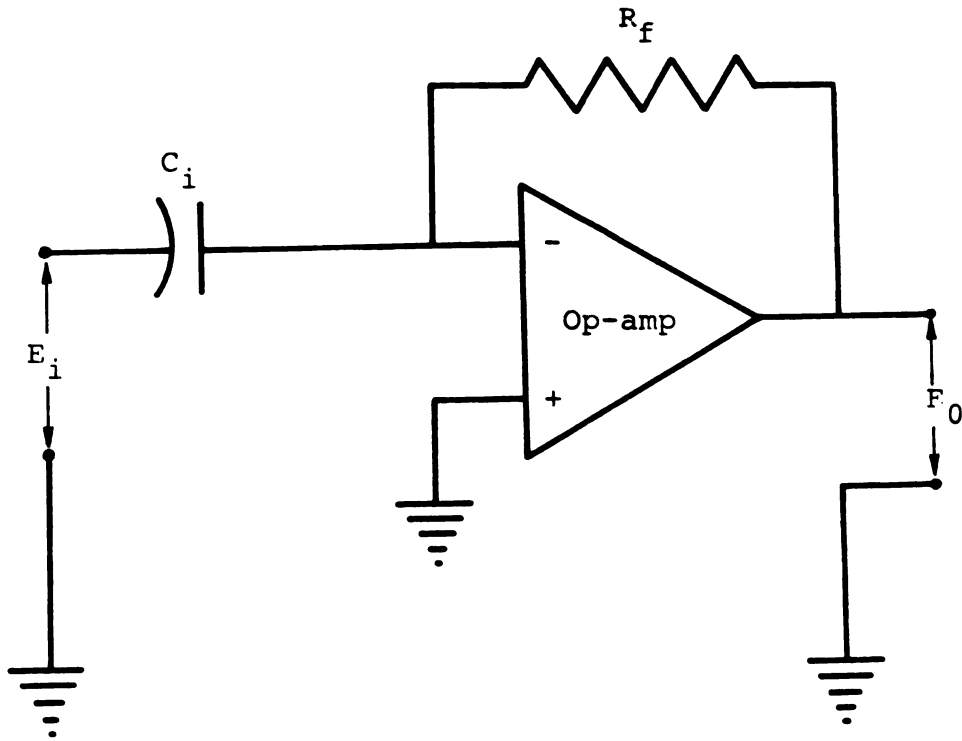


Figure 2.13. Strain signal trigger circuit.

of a free-ended rectangular plate. A schematic of an instrumented specimen prior to machining the slot is shown in Figure 2.14a. The consistence of the plane stress assumption is implied by the magnitudes of the response of gages 2 and 12 in Figure 2.15. Also, Figure 2.15b shows that there is little bending; note that the gages are separated by one inch in the longitudinal direction. The signals in Figure 2.15 show a longer rise-time than the later results as they were taken during development of the impact apparatus.

Dispersion, induced by finiteness of geometry, will alter the rise time and amplitude of a propagating step wave. The desire to generate a tensile pulse with a short rise time necessitated the use of a flat ended impactor for the present investigation. A flat ended impactor produces a pulse with a short rise time so that the shorter wave length components are more significant and therefore, according to the Pockhammer-Chree theory as discussed by Davies [67], the dispersive effects are greater. This phenomena poses a problem. Due to the presence of a slot in the specimen one cannot measure the input pulse at the slot. On the other hand one can measure the pulse at a location one inch before the slot and assume dispersion to be negligible. The validity of this assumption is implied by the response of gages 2 and 12, which cover the region of interest, as shown in

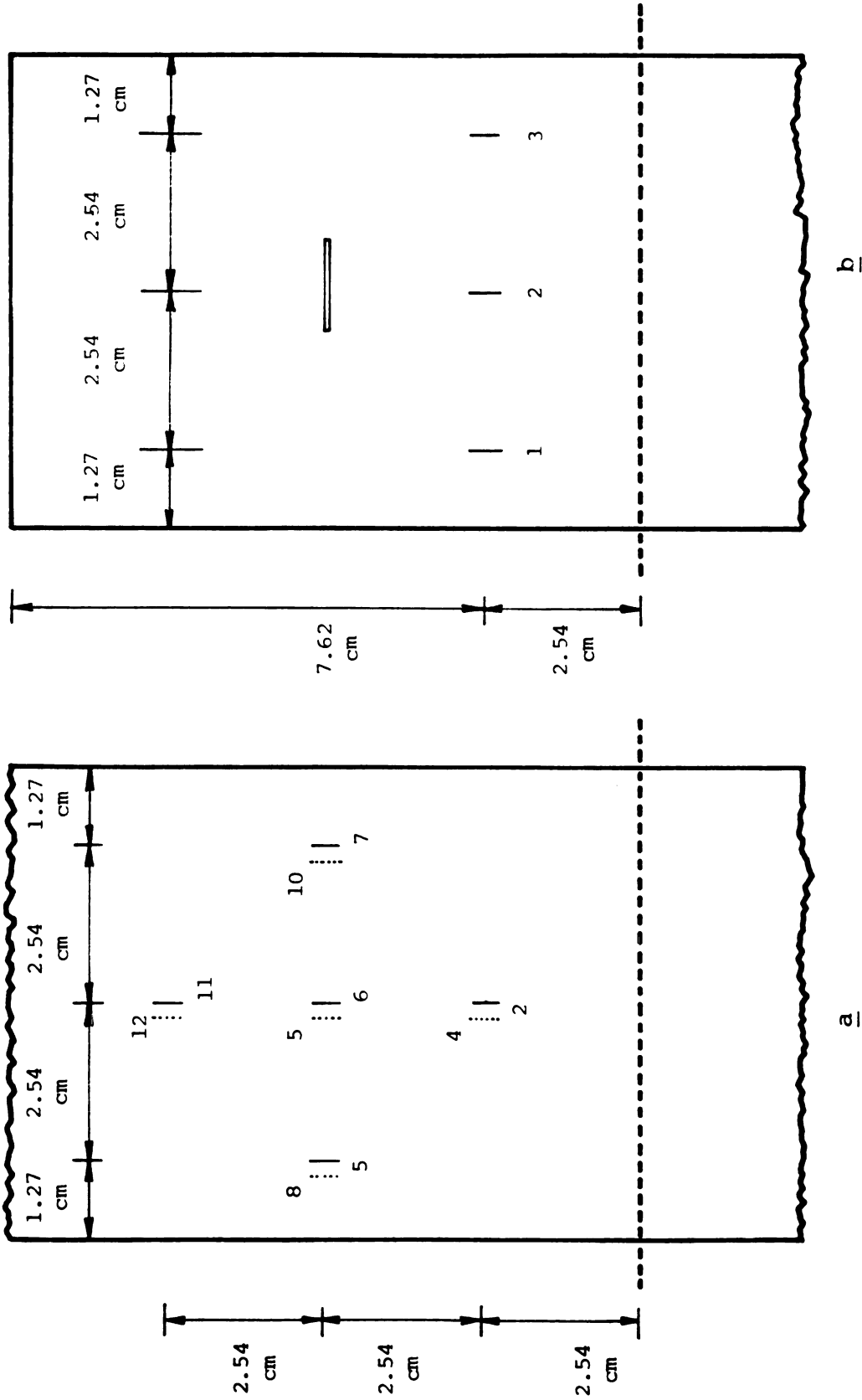


Figure 2.14. Strain gage locations on the specimen before and after machining the slot.

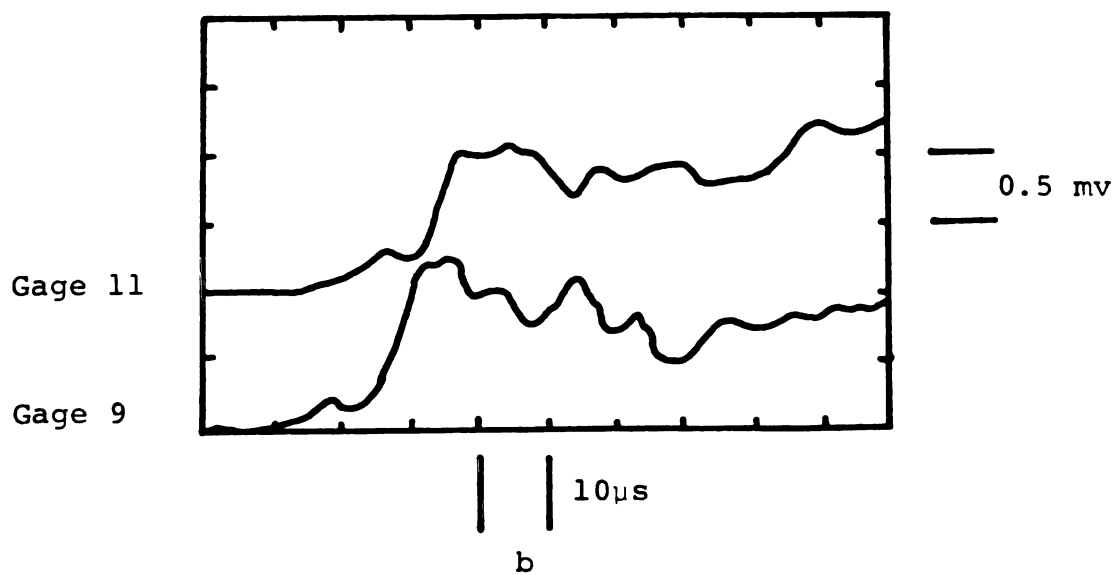
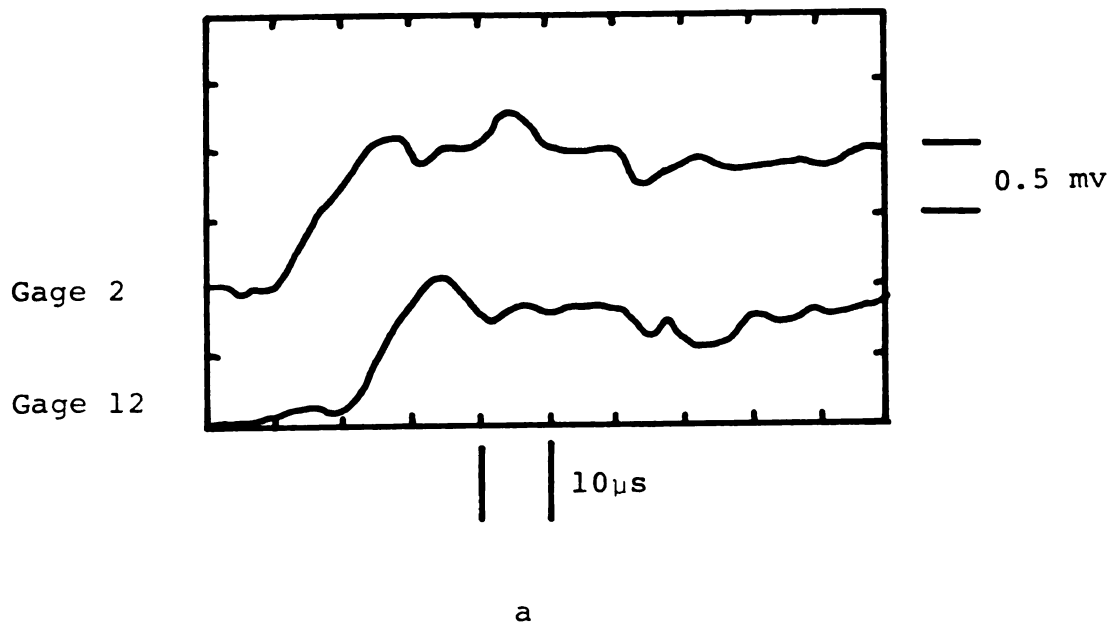


Figure 2.15. Observed strain response at various locations of the specimen without the slot.

Figure 2.14a. Note that even though the change in amplitude and rise time are negligible the oscillations in the pulse are indicative of some dispersive effects.

An air-cushion between the impactor and the tup would increase the strain pulse rise-time in the specimen. In order to eliminate the air-cushion, the tensile impact apparatus was designed such that a vacuum could be drawn in the launch tube. Great care was taken in sealing the launch tube. Even then leakage was unavoidable. Tests with slightly reduced launch tube pressures showed no improvement of the strain pulse rise time. The attempt to draw a vacuum in the launch tube was then discontinued.

B. Eccentricity of Loading

Since the primary objective of the present investigation was to study the response of the interaction of a longitudinal wave of normal incidence with a crack, particular care was taken to reduce the eccentricity in the apparatus. Further provision was made to check the planarity of the pulse during the actual test by observing if gages such as one and three in Figure 2.14b respond simultaneously to the wave front. It was then found that the axiality problem was worse than expected - a few percent of all impacts being axial to within two microseconds. Another problem observed during the course of testing was an occasional vertical non axial impact. This, in most cases was a result of bolts loosening in the tup or the projectile assembly.

C. Testing Procedure

The potentiometric strain gage circuits, the amplifiers, the oscilloscopes, the laser and photomultiplier power supplies were turned on at least one-half hour before a test was performed in order to obtain nearly steady state operating conditions.

The procedure adopted in testing was as follows:

- 1) The oscilloscopes with plug-in preamplifiers were calibrated for amplitude by means of the square-wave calibrator output incorporated in the oscilloscope. The sweep rate of the oscilloscope was calibrated with one, five and fifty microseconds timing marks from a time mark generator. These calibrations were performed against a graticule-scale over the face of the cathode ray tube.
- 2) The test specimen was carefully mated with the tup assembly. The bolts in the clamping brackets were tightened to secure the test specimen which is now sandwiched between the two brass bars of the tup assembly. The entire assembly was then mounted on the end of the launch tube and the projectile assembly pulled back and aligned against the accelerating assembly.
- 3) The incident laser beam was aligned so that the indentations are illuminated at the beginning of loading and throughout the test. This is done using the

adjusting screws on the mirror directing the beam. The specimen reflects a portion of the incident beam on the laser head. In order to insure the perpendicularity of the incident beam the reflection on the laser head was used as a guide in adjusting the laser position.

- 4) The photomultiplier tubes were positioned so that the fringe patterns fall on the windows. This was accomplished using the travelling stages which angularly orient the photomultiplier tubes. Further adjustments were made by rotating the windows of the photomultiplier tubes so that the fringes are parallel to the slits.
- 5) The oscilloscopes were set on single sweep lockout so that the entire test was recorded on one sweep. This required a sweep rate of five microseconds/cm. The sweep for the fringe motion record was triggered by a signal from a strain gage mounted about a quarter of an inch behind the impacting interface. The type 551 oscilloscope was triggered using a delay triggering signal from the Type 555.
- 6) The vertical gain adjustments of the amplifiers were set as desired in accordance with the particular test.
- 7) A set pressure was applied to the forward chamber of the Hyge unit and locked in.
- 8) The camera shutters were opened and held open until after the Hyge unit fired.

- 9) The Hyge load pressure was gradually increased until firing.
- 10) The load pressure was released and the Hyge piston was retracted to be ready for the next test.
- 11) The potentiometric strain gage circuit voltage was read and recorded.
- 12) The projectile assembly was pulled back and aligned for the next test.
- 13) The procedure 3 through 12 was repeated for the three sets of indentations.

CHAPTER III

ANALYSIS OF CRACK RESPONSE TO LONGITUDINAL PLANE WAVES OF NORMAL INCIDENCE

3.1 ANALYTICAL CONSIDERATIONS

A. Equations of Elasticity in Two Dimensions

Consider the problem depicted in Figure 3.1. The plate which is assumed isotropic linear elastic has the width $2b$, where $b \gg h$. The displacement components are U_x , U_y , and U_z in the x , y and z directions respectively. Since the plate is thin and free from stresses at surface $z = \pm h$, we assume

$$\sigma_z = \tau_{yz} = \tau_{xz} = 0 \quad (3.1)$$

In the absence of body force, integrating the three-dimensional stress equation of motion across the thickness of the plate, and ignoring transverse inertia as well as the integrations across the thickness of the plate of the transverse shear stresses, give

$$\begin{aligned} \frac{\partial \sigma_x}{\partial x} + \frac{\partial \tau_{xy}}{\partial y} &= \rho \frac{\partial^2 U_x}{\partial t^2} \\ \frac{\partial \tau_{xy}}{\partial x} + \frac{\partial \sigma_x}{\partial y} &= \rho \frac{\partial^2 U_y}{\partial t^2} \end{aligned} \quad (3.2)$$

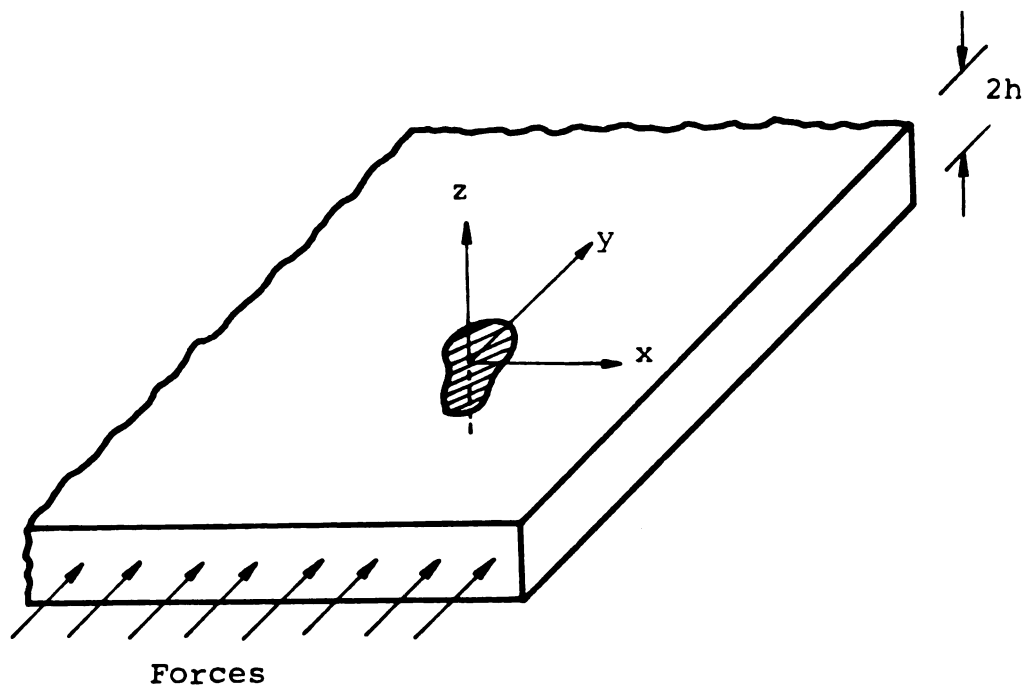


Figure 3.1. Geometry for generalized plane stress.

In these equations the field variables represent averages across the thickness of the plate, and ρ is the mass density. A similar averaging process gives the average field variables for the stress-strain relations and strain-displacement relations as

$$\begin{aligned}\sigma_{ij} &= \lambda \epsilon_{kk} \delta_{ij} + 2\mu \epsilon_{ij} \\ \epsilon_{ij} &= \frac{1}{2}(U_{i,j} + U_{j,i})\end{aligned}\quad i, j = 1, 2, 3 \quad (3.3)$$

where λ and μ are the Lamé's constants and δ_{ij} is the Kronecker delta.

From Hooke's Law it follows that ϵ_{33} is related to $\epsilon_{11} + \epsilon_{22}$ by

$$\epsilon_{33} = -\frac{\lambda}{\lambda + 2\mu} U_{k,k} \quad (3.4)$$

Substitution of (3.4) into the expression for the stress yields

$$\begin{aligned}\sigma_{\alpha\beta} &= \frac{2\mu\lambda}{\lambda + 2\mu} U_{k,k} \delta_{\alpha\beta} + \mu(U_{\alpha,\beta} + U_{\beta,\alpha}) \\ \alpha, \beta &= 1, 2\end{aligned}\quad (3.5)$$

which may be expanded as

$$\begin{aligned}\sigma_x &= \rho C_p^2 \left[\frac{\partial U}{\partial x} \frac{x}{x} + \nu \frac{\partial U}{\partial y} \frac{y}{y} \right] \\ \sigma_y &= \rho C_p^2 \left[\frac{\partial U}{\partial y} \frac{y}{y} + \nu \frac{\partial U}{\partial x} \frac{x}{x} \right] \\ \tau_{xy} &= \rho C_s^2 \left[\frac{\partial U}{\partial y} \frac{x}{x} + \frac{\partial U}{\partial x} \frac{y}{y} \right]\end{aligned}\quad (3.6)$$

where,

$$C_p^2 = \frac{4\mu(\lambda + \mu)}{\rho(\lambda + 2\mu)}$$

$$C_s^2 = \mu/\rho \quad \nu = \text{Poisson's ratio}$$

By substituting Equation (3.6) into Equation (3.2) the displacement equations of motion for a thin plate are reduced to

$$(C_p^2 - C_s^2) \nabla \nabla \cdot \bar{U} + C_s^2 \nabla^2 \bar{U} = \ddot{\bar{U}} \quad (3.7)$$

where \bar{U} is the displacement vector having two components, U_x and U_y in x and y directions, respectively. The symbol ∇ represents the gradient operator in two dimensions. The dot over the displacement \bar{U} denotes the time derivative, and ∇^2 is the two-dimensional Laplacian operator.

Let \bar{a} be a unit vector normal to the median plane of the plate. By introducing a scalar displacement potential ϕ and a vector displacement potential $\bar{\psi} = \bar{a}\psi$ and taking

$$\bar{U} = \nabla \phi + \nabla_{\mathbf{x}} \bar{\psi} \quad (3.8)$$

which may be expanded as

$$\begin{aligned} U_x &= \frac{\partial \phi}{\partial x} + \frac{\partial \psi}{\partial y} \\ U_y &= \frac{\partial \phi}{\partial y} - \frac{\partial \psi}{\partial x} \end{aligned} \quad (3.9)$$

Equation (3.7) can be reduced to two scalar wave equations

$$C_p^2 \nabla^2 \phi = \ddot{\phi} \quad (3.10)$$

$$C_s^2 \nabla^2 \psi = \ddot{\psi} \quad (3.11)$$

The stress-displacement relation may be used to give

$$\begin{aligned} \sigma_x &= \lambda' \nabla^2 \phi + 2\mu \left(\frac{\partial^2 \phi}{\partial x^2} + \frac{\partial^2 \psi}{\partial x \partial y} \right) \\ \sigma_y &= \lambda' \nabla^2 \phi + 2\mu \left(\frac{\partial^2 \phi}{\partial x \partial y} - \frac{\partial^2 \psi}{\partial x \partial y} \right) \\ \tau_{xy} &= \mu \left(\frac{2\partial^2 \phi}{\partial x \partial y} - \frac{\partial^2 \psi}{\partial x^2} + \frac{\partial^2 \psi}{\partial y^2} \right) \end{aligned} \quad (3.12)$$

where,

$$\lambda' = \frac{2\lambda\mu}{\lambda + 2\mu}$$

Equations (3.7) are Poisson's equations of extensional vibration of thin plates and constitute the dynamical counterpart of the equations of generalized plane stress. They are the zero-order approximation of the three dimensional equation of elasticity as the displacement components are assumed to be independent of the thickness coordinate of the plate. As pointed out by Mindlin [68], the zero-order equations do not contain the simple thickness modes, hence they are limited to frequencies well below the frequencies of the thickness-stretch and symmetric thickness-shear modes which are

$$\omega = [(\pi/h)(\lambda + 2\mu)/\rho]^{1/2}, \quad \omega = (2\pi/h)(\mu/\rho)^{1/2} \quad (3.13)$$

respectively, where h is the thickness of the plate. In addition, because of the omission of the low-frequency portions of the complex branches of general waves in a plate, the equations require the wave length to be large in comparison with the thickness of the plate. Thus the approximation is valid when the frequency is less than c_s/h and when the wave length is longer than πh .

For an impact loading the approximate solutions can be expected to be valid at some distance from the edge, based on the observation that in the far field the low frequency-long waves contributions of the lowest mode dominates the contribution of the other modes.

B. Formulation of the Problem

Consider an isotropic linear-elastic plate containing a crack. A rectangular coordinate system x, y, z is oriented as shown in Figure 3.2, so that the z axis coincides with one edge of the crack. For a plane tension-stress wave propagating in the positive y -direction into the initially undisturbed material $U_x = 0$ and only one wave potential $\phi(y,t)$ is required to describe the wave motion.

As the incident plane wave impinges on the crack the path of the wave propagation is changed and the crack, when excited by the otherwise undisturbed wave, acts as

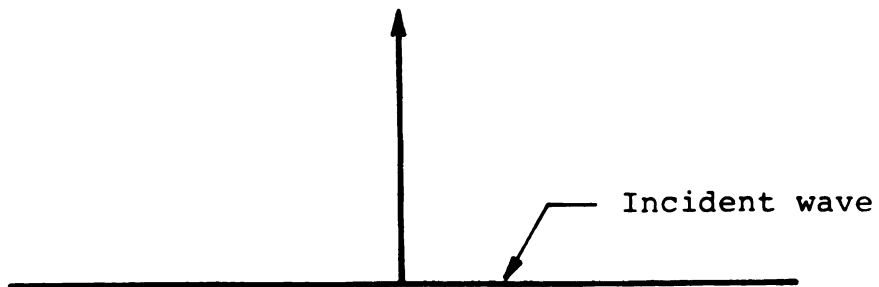
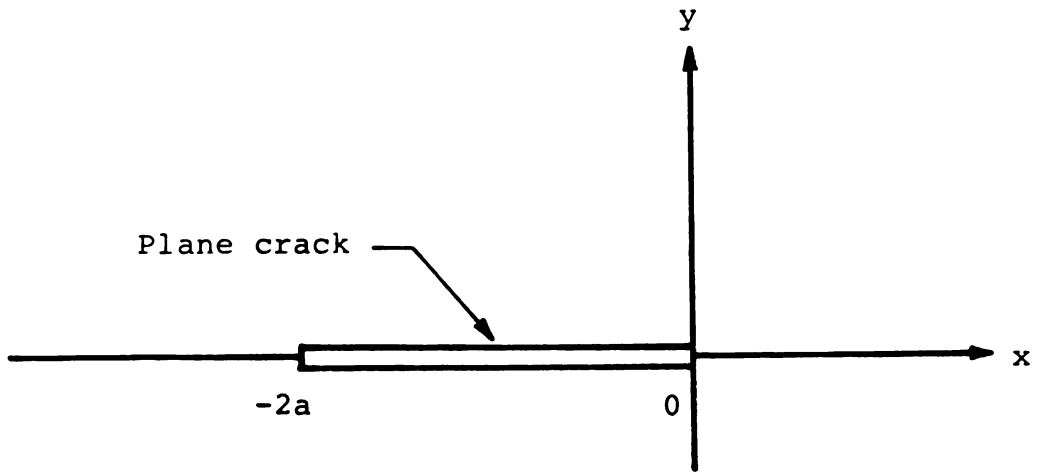


Figure 3.2. Geometry of the problem.

a secondary source which emits waves outward from itself. The deviation of the wave from its original path is known as diffraction, and the spawning of secondary waves from the crack is known as scattering. In the equations that follow superscripts i and s indicate incident and scattered waves respectively.

The incident plane wave normal to the crack may be represented as

$$\phi^i = f(t - y) \quad (3.14)$$

$$\psi^i = 0 \quad (3.15)$$

where f is identically zero when its argument is negative, but otherwise is an arbitrary waveform. Thus the initial time for the problem is when the wave reaches the crack, $y = 0$. Ahead of the advancing plane front the plate is undisturbed.

Substitution of Equations (3.14) and (3.15) into (3.12) gives the stresses of the incident longitudinal plane waves as

$$\sigma_x^{(i)} = (\kappa^2 - 2)f'' \quad (3.16)$$

$$\sigma_y^{(i)} = \kappa^2 f'' \quad (3.17)$$

where the elastic constant $\kappa^2 = \left(\frac{C_P}{C_S}\right)^2$ takes the value $2/(1 - \nu)$ in this case and primes indicate differentiation with respect to the argument. To compare the analytical results with experiment, f'' will be chosen to approximate the pulse generated experimentally.

Since both Equations (3.14) and (3.15) are already solutions of the wave equations, the main burden of the analysis is to determine the potentials $\phi^{(s)}$ and $\psi^{(s)}$ of the scattered wave field. The scattered waves which are added to the incident waves to form the total field are determined from Equation 3.12 and the boundary conditions

$$\begin{aligned}\sigma_y^{(i)}(x,0) + \sigma_y^{(s)}(x,0) &= 0 & -2a < x < 0 \\ \tau_{xy}^{(i)}(x,0) + \tau_{xy}^{(s)}(x,0) &= 0 & -2a < x < 0\end{aligned}\tag{3.18}$$

which specify that the crack surfaces are separated and free of traction.

C. Solution of Problem

In the preceding section we described the problem of the diffraction of an arbitrary transient plane wave by a crack normal to the propagation direction. Although the solution of this problem is not known, the analytical results for a similar problem with a step function stress profile have been obtained by many researchers; a brief review of which was given in Chapter I. Thau and Lu [16] considered a plane dilational wave of arbitrary profile impinging on a stationary line crack at an arbitrary angle. They used the generalized Wiener-Hopf technique, which yields an iteration series solution that is exact for a finite time which increases with each

increasing order of iteration. They present explicit expressions for the dynamic normal and shear stress intensity factors at each crack tip as a function of time, angle of incidence and Poisson's ratio. Furthermore, they present numerical results for the dynamic normal and shear stress intensity factors which are exact for two crack transit times and the dynamic crack surface separation at several points that is exact for one crack transit time. These numerical results are for an incident wave with a step function stress profile. In this analysis the material was considered linear-elastic, homogeneous, isotropic, and infinite so that conditions of plane strain prevail.

According to the theory of elastodynamics, a plane strain solution can be transformed into a plane stress solution by merely changing the ratio of wave speeds $\kappa = 2(1 - \nu)/(1 - 2\nu)$ of the plane strain solution to $\kappa = 2/(1 - \nu)$. In other words, the analytical results of the diffraction of a plane step-longitudinal wave by a crack in an unbounded elastic medium may be utilized to obtain the solution for the corresponding diffraction problem in a thin plate. The value of Poisson's ratio measured for the test specimen was $\nu = 0.33$ which corresponds to a plane strain $\nu = 0.25$. Thus, the results of the mode I stress intensity factor and the crack surface separation for $\nu = 0.25$ in Figures

3 and 2 of reference [16] can be used as an influence function to determine the theoretical stress intensity factor and crack displacement by a wave with an arbitrary time variation.

Let $U_s(x, t - t')$ denote the vertical separation of the crack faces at a point x on the crack at time t due to a unit step stress pulse which strikes the crack at time t' and $U_a(x, t)$ to be that for an arbitrary stress pulse. The experimentally generated stress pulse has a rise time form given by $f(t)$, determined experimentally from strain measurement, then elastodynamic theory predicts a vertical separation of the crack faces $U_a(x, t)$ given by Duhamel's integral:

$$U_a(x, t) = \int_0^t f(t') \frac{\partial}{\partial t} U_s(x, t - t') dt' \quad (3.19)$$

Use of (3.19) requires that an accurate means of determining $\frac{\partial U_s}{\partial t}$ is available, and that the crack does not close in the time interval $(0, t)$. Thau and Lu [16] give theoretical evidence of this assumption.

Noting that $\partial U_s(x, t - t')/\partial t = -\partial U_s(x, t - t')/\partial t'$, (3.19) may be integrated by parts to obtain

$$U_a(x, t) = f(0)U_s(t) + \int_0^t \frac{\partial}{\partial t'} f''(t')U_s(x, t - t') dt' \quad (3.20)$$

Equation (3.20) permits use of plots $U_s(x, t)$ directly provided that df/dt can be accurately determined from the experiment.

A similar use of the principal of superposition may be employed to determine the normal stress intensity factor due to an arbitrary $f(t)$

$${}_a k_1(t) = f(0) {}_s k_1(t) + \int_0^t {}_s k_1(t - t') \frac{\partial}{\partial t'} f(t') dt' \quad (3.21)$$

where ${}_s k_1(t)$ and ${}_a k_1(t)$ are the normal stress intensity factors due to a unit step stress wave and an arbitrary stress pulse respectively.

Plots of $U_s(x,t)$ for normal incidence are given in Reference [16] on page 744 (where it is denoted by $h_T^{(0)}$ for various values of x). These values are valid for one crack transit time. The plots of ${}_s k_t(t)$ given in Reference [16] on page 745 are valid until the first scattered longitudinal wave travels to the other crack tip and back again.

In order to evaluate the foregoing integrals numerically it was necessary to plot the tension-stress (strain) pulse $f(t)$ and the influence functions $U_s(x,t)$ and ${}_s k_1(t)$ on a common time scale. Reference [16] gives $U_s(x,t)$ in terms of the ratio $h_T^{(0)} = \frac{2a\tau}{\mu}$, where $\kappa^2 \tau_0$ is the normal stress associated with incident wave, and ${}_s k_1(t)$ in terms of the ratio ${}_s k_1(t) / \kappa^2 \tau_0 \sqrt{a}$, where $\kappa^2 \tau_0 \sqrt{a}$ is the static stress intensity factor. Furthermore, both $U_s(x,t)$ and ${}_s k_1(t)$ as a function of dimensionless abscissa $Ct/2$, where C is the velocity of propagation of the wave, $2a$ is the

crack length, and t is the time after the wave reaches the crack. For this analysis the value of C_p , measured velocity of propagation of the wave, was substituted for C .

The results of this analysis are compared with the experimental results in Chapter IV.

3.2 EXPERIMENTAL DATA CONSIDERATIONS

A. Strain Time History of the Incident Wave

Measurements of the strain-pulse amplitude and rise-time were taken from the photographic records using a Pye two-dimensional traveling microscope accurate to 0.01 millimeter. The relation between the change of resistance produced in a foil gage and the strain due to an applied load is given by

$$\Delta R_g / R_g = \epsilon F \quad (3.22)$$

where F is the gage factor and ϵ is the applied strain. The strain can be determined from the strain gage potentiometer-circuit output-voltage by the use of Equations (2.9) and (3.22). Multiplying the right hand side of Equation (2.9) by R_g / R_g and applying Equation (3.22) we have

$$E_0 = \frac{R_b R_g}{(R_b + R_g)^2} F E \epsilon \quad (3.23)$$

The readings from the photographic records with the use of the travelling microscope were used to

determine the amplitude deflection of the strain-pulse trace. The value of E_0 was then calculated with the following equation.

$$E_0 = \Delta_{\epsilon} G_{\epsilon} \quad (3.24)$$

where Δ_{ϵ} is the trace deflection in divisions and G_{ϵ} is the oscilloscope vertical-amplifier gain in volts per division.

The strain-pulse rise-time was calculated with the following equation

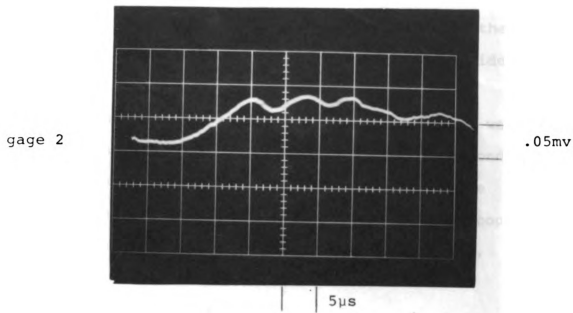
$$t_t = \Delta_t G_t \quad (3.25)$$

The readings from the photographic records with the use of the travelling microscope were used to determine the rise-time deflection, Δ_t in divisions, of the strain pulse trace. The oscilloscope horizontal-amplifier gain was G_t in seconds per division.

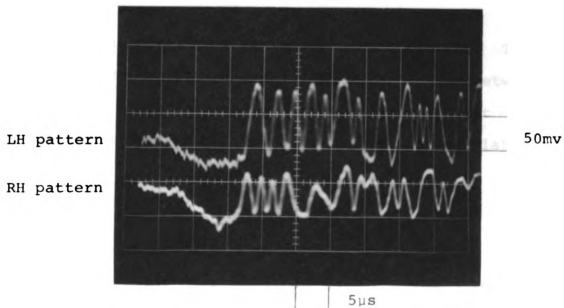
The strain time history so obtained could be converted to stress time history with the use of stress strain relations.

B. Dynamic Separation of Crack Faces

The dynamic displacements at various locations of the crack were determined using fringe motion records. A typical photograph of the recorded signals from an impact test is shown in Figure 3.3. The upper trace records the fringe pattern of the left-hand-side pattern



a. Strain-time history of the input pulse.



b. Oscilloscope photograph of fringe pattern signals

Figure 3.3. Experimental records for crack displacement at X_1 ($a/b = 0.54$).

(pattern furthest from the impact interface), and the lower trace records the motion of the right-hand-side pattern.

Fringe motion, δm , values of $0, \frac{1}{2}, 1, 1\frac{1}{2} \dots$ were read from the photographic records and the corresponding times (times at which maxima and minima occur) were read with the PYE two-dimensional measuring microscope. Once this was done for both traces Equation (2.13), which is

$$\delta d = \frac{\lambda_0}{\sin \alpha_0} \delta m$$

was used to calculate displacement both for the upper and lower fringe patterns. The upper and lower fringe pattern displacement time curves were then plotted. The crack displacement is the average at a given time between these curves. The results of a typical displacement measurement are given in Figure 3.4 which was calculated from Figure 3.3.

C. Dynamic Stress Intensity Factor

Using Westergaard's method the elastostatic stresses at a point near the crack tips for the configuration shown in Figure 3.5 can be written as

$$\sigma_{ij} = \sigma_0 \left(\frac{\pi a}{2r} \right)^{\frac{1}{2}} f_{ij}(\theta) \quad (3.26)$$

where:

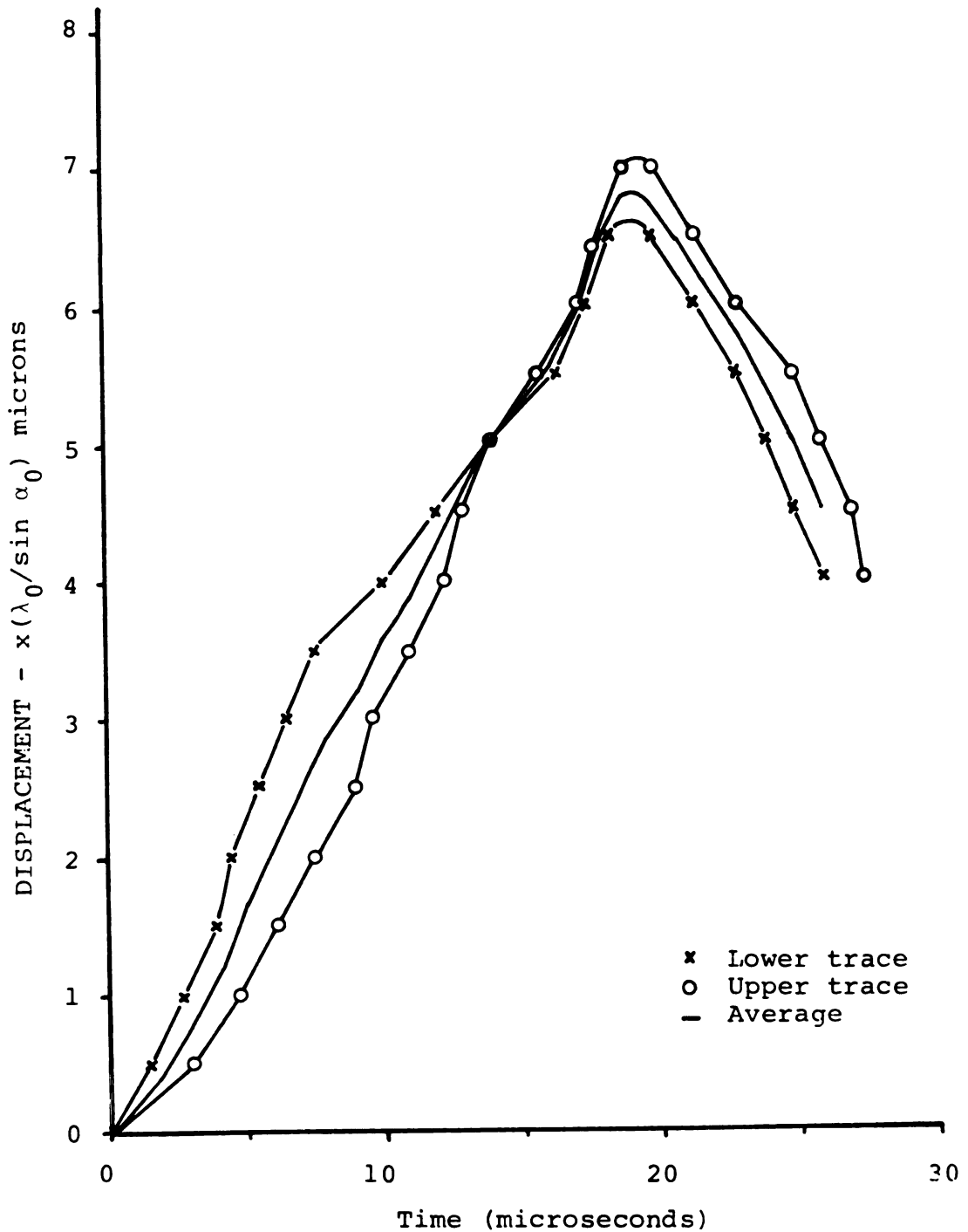


Figure 3.4. Results of crack tip opening displacement for the trimmed specimen showing the displacement associated with each fringe pattern.

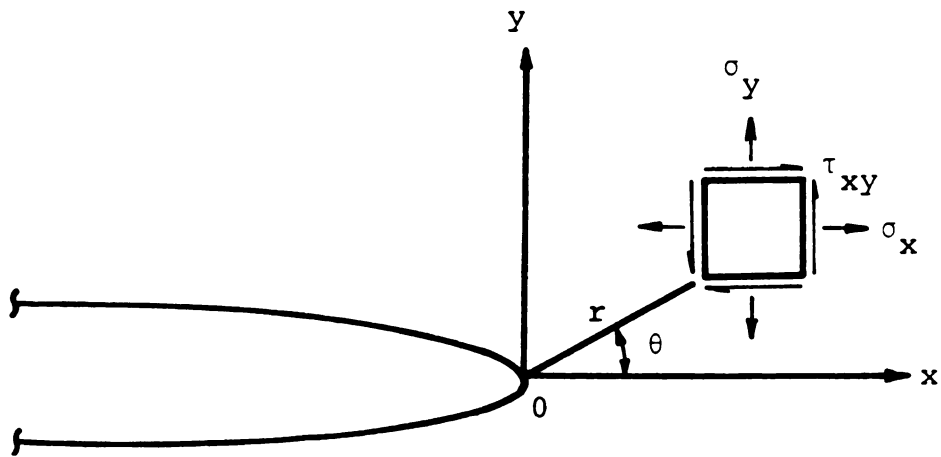


Figure 3.5. Local rectangular stress components.

$$f_x(\theta) = (1 - \sin \frac{\theta}{2} \sin \frac{3\theta}{2}) \cos \frac{\theta}{2}$$

$$f_y(\theta) = (1 + \sin \frac{\theta}{2} \sin \frac{3\theta}{2}) \cos \frac{\theta}{2}$$

$$f_{xy}(\theta) = f_{yx}(\theta) = \sin \frac{\theta}{2} \cos \frac{\theta}{2} \cos \frac{3\theta}{2}$$

i.e. for $r \ll a$.

Defining the mode I stress intensity factor

$$k_1 = \lim_{x \rightarrow 0} (2\pi r)^{\frac{1}{2}} \sigma_y(x, 0)$$

which for finite domains take the form

$$k_1 = \sigma_0 (\pi a)^{\frac{1}{2}} F(a/b)$$

where

$F(a/b)$ - a factor which can be considered as a finite-width correction to the infinite domain problem.

Then σ_{ij} can be written as

$$\sigma_{ij} = \frac{k_1}{(2\pi r)^{\frac{1}{2}}} f_{ij}(\theta) \quad (3.27)$$

Upon expansion

$$\sigma_x = \frac{k_1}{(2\pi r)^{\frac{1}{2}}} f_x(\theta)$$

$$\sigma_y = \frac{k_1}{(2\pi r)^{\frac{1}{2}}} f_y(\theta)$$

$$\tau_{xy} = \frac{k_1}{(2\pi r)^{\frac{1}{2}}} f_{xy}(\theta)$$

$$\sigma_z = \begin{cases} 0 & \text{for plane stress} \\ \nu(\sigma_x + \sigma_y) & \text{for plane strain} \end{cases}$$

If the crack under consideration is subjected to a longitudinal wave of normal incidence, the remote tensile stress, σ , is replaced by $\sigma_0 f(t)$ where σ_0 is the amplitude of the pulse. Thus, the components of stress and displacement near the crack tip become time dependent. We may consider that the local stress distribution in terms of the space variables, r and θ (see Figure 3.5) remains the same for all time, and that the only difference between a static and dynamic stress intensity factors is the time dependence.

Sih, Embley and Ravera [17] give components of dynamic stress in the neighborhood of a stationary crack as

$$\begin{aligned}\sigma_x &= \frac{k_1(t)}{(2a)^{\frac{1}{2}}} \cos \frac{\theta}{2} \left[1 - \sin \frac{(\theta)}{2} \sin \frac{(3\theta)}{2} \right] + \dots \\ \sigma_y &= \frac{k_1(t)}{(2a)^{\frac{1}{2}}} \cos \frac{\theta}{2} \left[1 + \sin \frac{(\theta)}{2} \sin \frac{(\theta)}{2} \right] + \dots \quad (3.28) \\ \tau_{xy} &= \frac{k_1(t)}{(2a)^{\frac{1}{2}}} \cos \frac{(\theta)}{2} \sin \frac{(\theta)}{2} \cos \frac{(3\theta)}{2} + \dots\end{aligned}$$

where

$$k_1 = \sigma_0 (a)^{\frac{1}{2}} F(a/b)$$

Comparisons of each of these expressions with expressions in Equation (3.26) show the similarity. Thus, the dynamic stress intensity factor may be defined in a manner analogous to the elastostatic theory

$$k_1(t) = \sigma_0 (\pi a)^{\frac{1}{2}} F(a/b) [1 + \Lambda(a,b,c,t)] \quad (3.29)$$

where,

σ_0 - amplitude of stress pulse

$F(a/b)$ - finite width correction factor

$\Lambda(a,b,c,t)$ - correction factor for the dynamic effect

Note that the time varying correction factor for the dynamic effects, $\Lambda(a,b,c,t)$, is dependent on the stress history, the crack length, the wave speed and the geometry of the specimen.

The dynamic crack opening near the tip for the case of plane stress is then given as

$$U_y^0(t) = \frac{k_1(t)}{G} \left(\frac{r}{2\pi}\right)^{\frac{1}{2}} \sin \frac{\theta}{2} \left[\frac{2}{(1+\nu)} - \cos^2 \frac{\theta}{2}\right] + \dots \quad (3.30)$$

It is this equation, measurement of the time varying crack opening $U_y^0(t)$ and the polar coordinates r, θ (see Figure 3.5), that was used to calculate the dynamic stress intensity factor $k_1(t)$.

D. Dynamic Crack Profile

The dynamic crack profile at various times was determined from experimental data. The measure of crack displacement at various locations (near the tip, a quarter crack length from the tip, and at half the crack length from the tip) for a given time step as read from displacement-time curves determined in a manner described in section B was used. These values were then used to

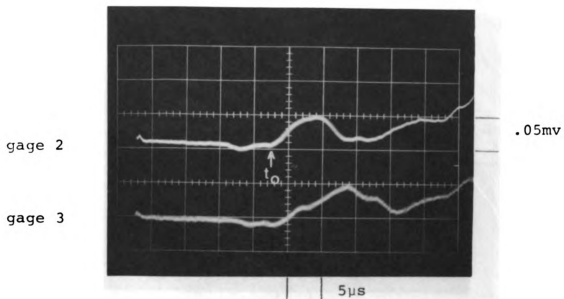
plot a curve of crack displacement versus distance from crack tip. The process was repeated for several time steps. Thus resulting a dynamic crack profile.

CHAPTER IV
RESULTS AND COMPARISON WITH THEORY

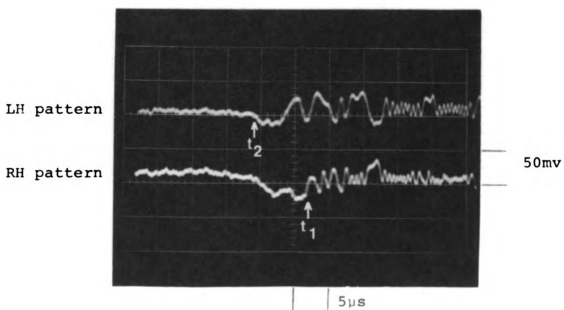
4.1 EXPERIMENTAL RECORDS

The experimental records for strain pulses and corresponding fringe motion signals at x_3 , x_2 and x_1 are shown in Figures 4.1, 4.2, and 4.3. The time scale reads from left to right in these photographs.

Strain pulse records for three tests are shown in Figures 4.1a, 4.2a, and 4.3a. The upper trace in each record is the output from gage station two at the center of the specimen while the lower trace is from gage station three at the side. The first upward-going portion of the traces are the initial tension pulses produced by the impact. The first dip in the trace is due to the reflected wave from the free surface of the crack. The slight deviations in the amplitudes can be attributed to two factors. One is the variation of the impact velocity. The launch tube clearance was .05 cm, and the Hyge was always fired at a set pressure of .04 MPa. However, the air flow past the impactor could cause the impact assembly to intermittently graze the side of the launch tube. This may have resulted in an intermittent friction force acting on the impact assembly that would change the impact velocity

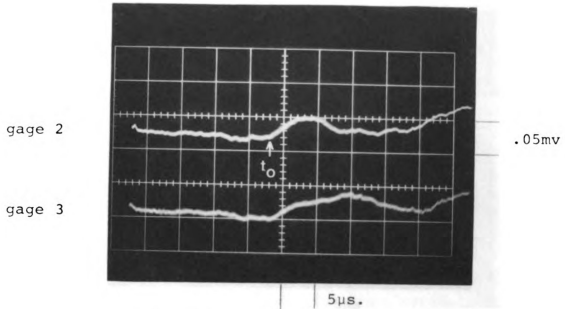


a. Strain-time history of the input pulse.

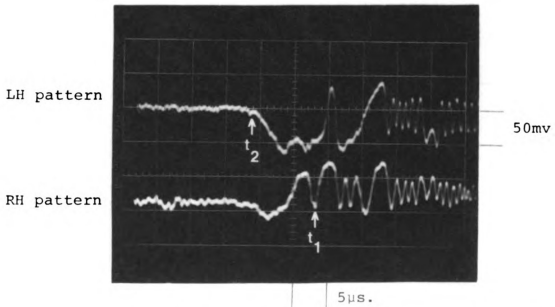


b. Oscilloscope photograph of fringe pattern signals.

Figure 4.1. Experimental records for crack displacement at X_3 ($a/b = 0.167$).

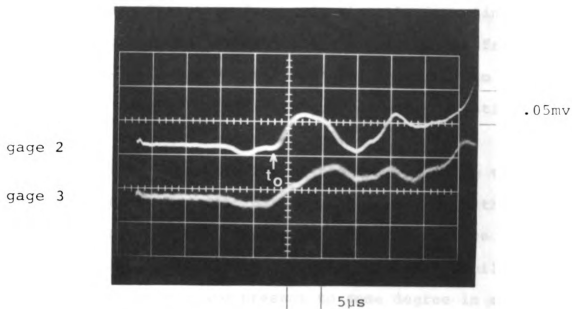


a. Strain-time history of the input pulse.

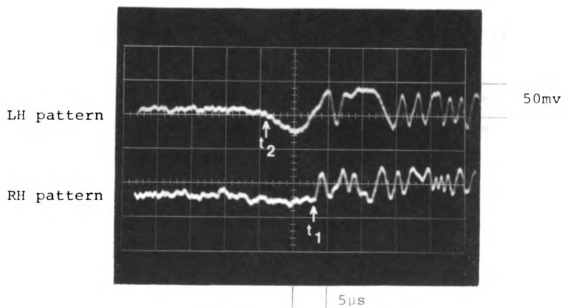


b. Oscilloscope photograph of fringe pattern signals.

Figure 4.2. Experimental records for crack displacement at X_2 ($a/b = 0.167$).



a. Strain-time history of the input pulse.



b. Oscilloscope photograph of fringe pattern signals.

Figure 4.3. Experimental records for crack displacement at X_1 ($a/b = 0.167$).

between tests. The other factor is that the impacting interface experienced a slight plastic deformation from each impact. This caused the impacting interface to deviate from smooth surfaces, thereby causing variations in the pulse amplitude and rise-time.

A critical examination of the time at which the strain pulses of gage stations two and three reach their maximum for a given test suggests a slight curvature in the wave front. It is interesting to note that similar wave front curvatures are present to some degree in all the full field dynamic photoelastic fringe patterns which have been obtained for longitudinal impact of rectangular bars. Curvatures of the leading edges are observed in the pictures of Durelli, et al. [69], [70] and Feder et al. [71].

Figures 4.1b, 4.2b, and 4.3b are photographs of recorded signals for fringe pattern at test stations x_3 , x_2 , and x_1 respectively. For each photograph the upper trace records the fringe pattern of the left-hand-side pattern (pattern furthest from the impact interface), and the lower trace records the right-hand-side pattern.

The initial displacement of the indentations is caused by the leading edge of the wave front which travels at the elastic wave velocity in the specimen. On the right-hand signal, the fringe motion due to relative displacement is opposite that due to rigid body motion, whereas

for the left-hand one they add together. This results in a delay in time for the right-hand signal to move from its zero position, but the left-hand signal moves as soon as small displacement signals arrives.

The starting time for the strain pulse is taken to be the first deviation from the zero level of the upward-going signal at station two, i.e. t_0 in Figures 4.1a, 4.2a, and 4.3a. The small disturbances before t_0 are caused by imperfections of the impacting faces; the loading mechanism doesn't generate a perfect ramp, but generates a precursor pulse and a main pulse. Station two is one inch ahead of the crack; therefore, the starting time for fringe motion measurements is 5 microseconds later, i.e. t_1 in Figures 4.1b, 4.2b, and 4.3b.

Ideally, the output signals from the photo-multiplier tube would be sine waves about an unchanging zero position. This does not occur because of the degradation of the fringe pattern due to reflections from irregular crack surfaces. The result is a pattern with streaks running through it.

The initial displacement of crack surfaces is small, but it increases as the wave front peak begins to arrive, as indicated by the increase in the fringe frequency. As the frequency increases, the amplitude decreases because of the limited frequency response of the system. This is of course, of no consequence to displacement measurement as long as the fringe peak can be

distinguished. The amplitude may also change as the indentations move within the incident laser beam.

The two abrupt changes of fringe signals in each record are due to reversals of displacement. There can be a certain ambiguity in the interpretation of this displacement interferometer data because, from the fringe record alone, there is no way of knowing whether or not an abrupt change in fringe signals is due to a single reversal or a double reversal. However, in practice, it is nearly always possible from the boundary conditions of the experiment to say with confidence how many displacement reversals, if any, there will be in the data, and at about what time they should occur.

The first abrupt change in the fringe signals takes place at about 15 microseconds from the first deviation from zero of the fringe patterns (t_2 in Figures 4.1b, 4.2b, and 4.3b) while the second takes place at about 24 microseconds. Based on specimen boundary conditions 12.5 microseconds from t_1 correspond to the time it takes for the scattered waves to travel from the crack tip to the nearest boundary and back to the tip while 20 microseconds correspond to the arrival time of the reflection from the free end of the specimen. This would then suggest that the abrupt changes in the fringe signals that take place at 15 microseconds from t_2 are due to a double reversal.

4.2 GENERAL CRACK BEHAVIOR

The results of typical displacement measurements are given in Figures 4.4, 4.5, and 4.6 which were calculated from Figures 4.1b, 4.2b, and 4.3b respectively. Two time scales are plotted here to show the effect of the precursor pulse and the main pulse.

The oscillations in displacement-time curves may be attributed to scattering phenomena from the crack tips and the boundary surfaces. Both effects have been considered in the literature. Sih, Embley and Ravera [17], who considered the problem of the diffraction of stress waves by a crack in an infinite medium, established that a damped oscillation should appear in the $\tilde{k}_1(t)$ -vs- t curve. This is, of course also true for a displacement-time curve. Chen [19] numerically analyzed the problem of a central crack in a finite bar and recognized the oscillations in the $\tilde{k}_1(t)$ -vs- t curve as being caused by the cancellation and reinforcement of the incident waves by various scattered waves. Furthermore, Chen introduced the time marks I, R, P and S (used in Figures 4.4, 4.5, and 4.6) to identify the oscillations in the $\tilde{k}_1(t)$ -vs- t curve. The symbols I, R, P, and S thus, denote the time-of-arrival at the crack tip of the longitudinal wave (I) and the subsequent Rayleigh wave (R) from the other tip and the nearest boundary reflections of pressure (P) and shear (S) waves respectively.

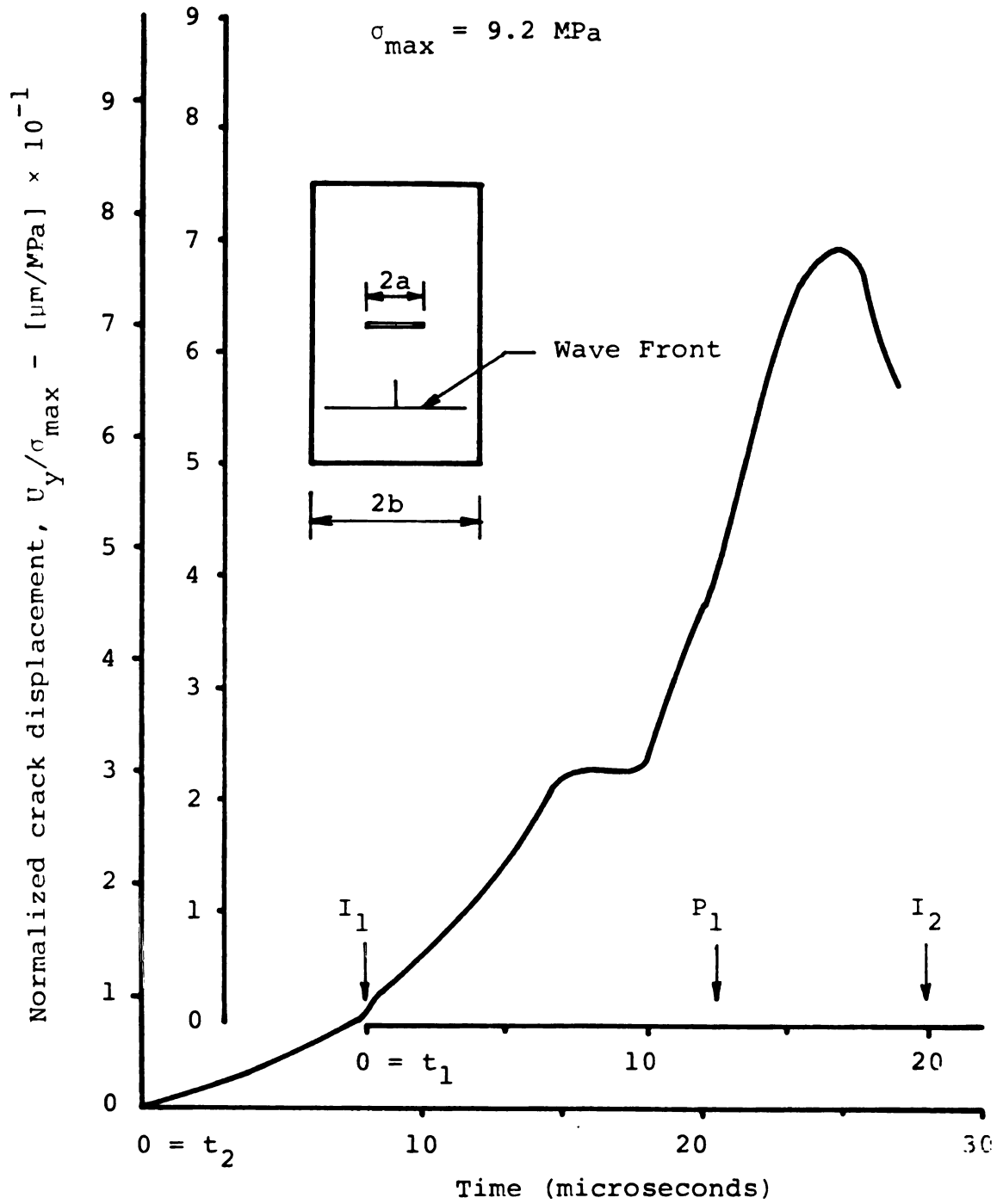


Figure 4.4. Variations of displacement at X_3 with time for specimen with $a/b = 0.167$.

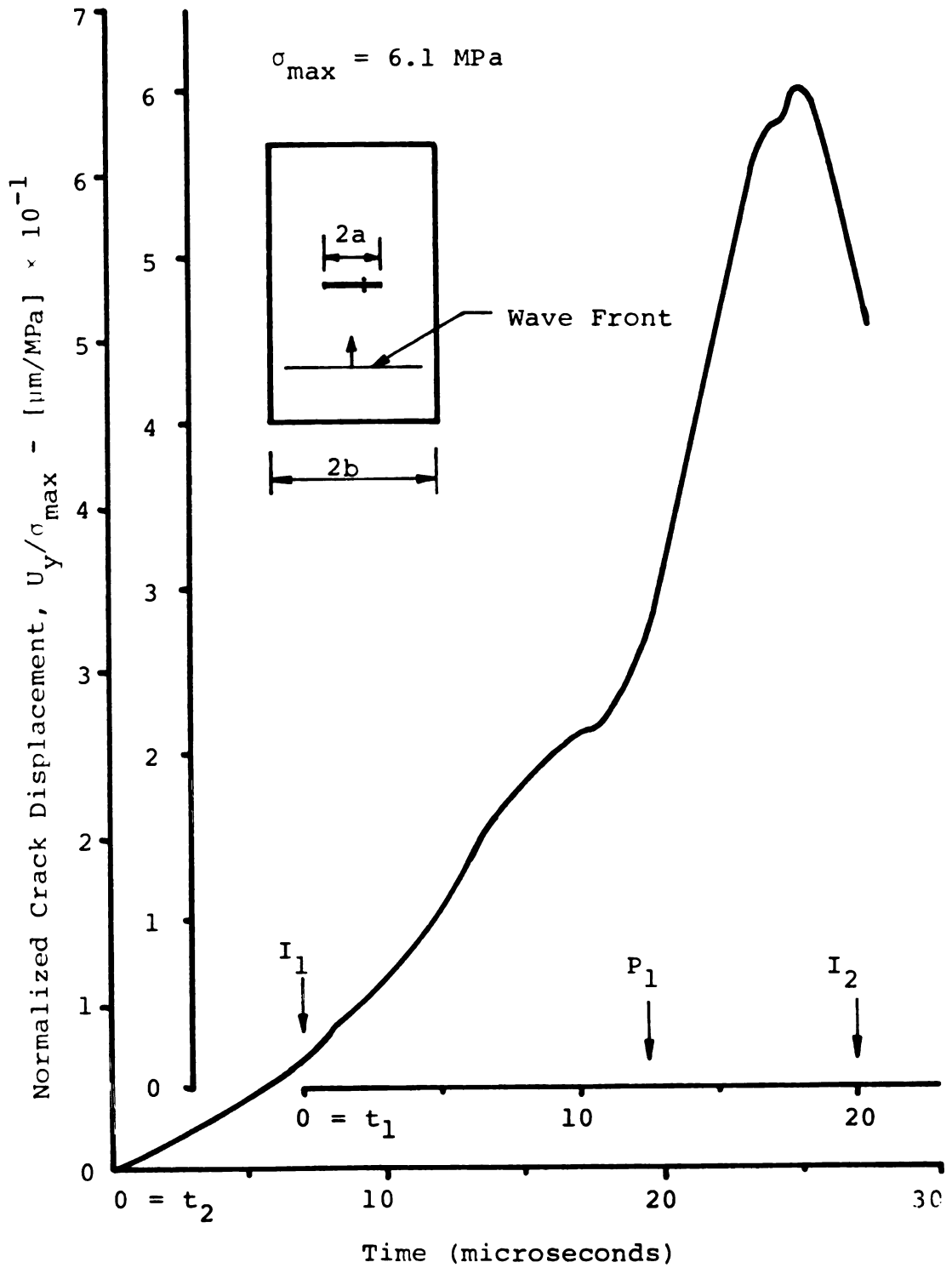


Figure 4.5. Variations of displacement at X_2 with time for specimen with $a/b = 0.167$.

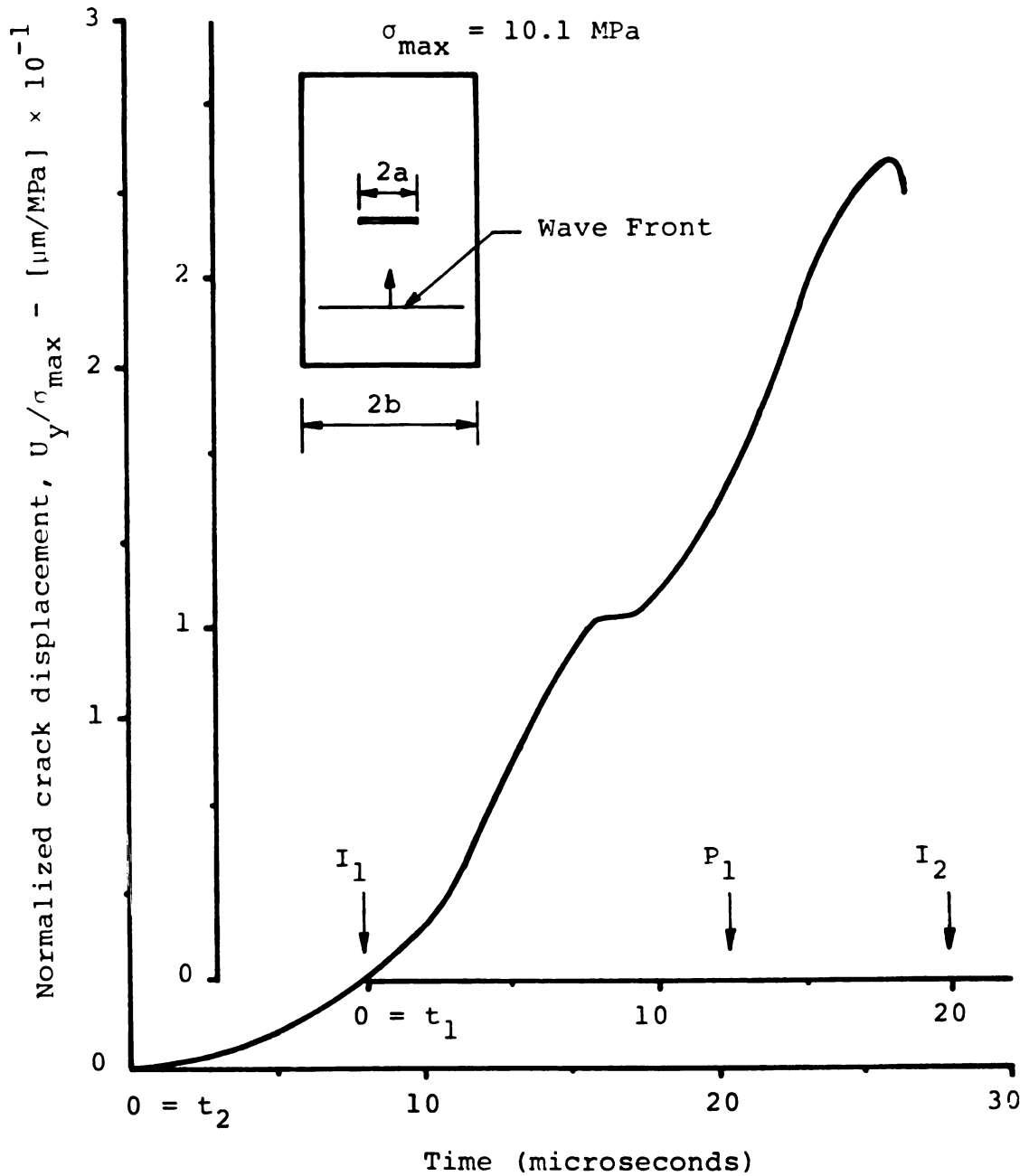


Figure 4.6. Variations of displacement at X_1 with time for specimen with $a/b = 0.167$.

Subscripts 1 or 2 on these symbols indicate association with the first or second arrival of the longitudinal wave.

As can be noted from Figures 4.4, 4.5, and 4.6 the results obtained here have the same general behavior as the $k_1(t)$ -vs- t or displacement-time curve of Reference [19]. Note that no experimental evidence exists for the high frequency oscillation that might be caused by the plate thickness, perhaps because of the length of the recording time.

Equation (3.30) and the crack tip displacement results were used to compute the mode I dynamic stress intensity factor, $k_1(t)$, for various values of times after the arrival of the wave front at the crack. The normalized mode I dynamic stress intensity factor, $\tilde{k}_1(t) = k_1(t)/\sigma_{\max}(\pi a)^{1/2}$ is plotted against time in Figure 4.7. As might naturally be expected the qualitative characteristics of the curve are similar to those of the crack displacements. Thus the time marks I, R, P and S may be used again to identify the oscillations in the $k_1(t)$ -vs- t curve as being caused by the cancellation and reinforcement of the incident waves by various scattered waves. The experimental result shows a $k_1(t)$ dynamic overshoot of 170% in contrast to numerical results of about 175% of Reference [19] which consider a Heaviside step loading of a crack in a steel bar with a/b ratio of 0.24 and Poisson's ratio of 0.3. The normalized static stress intensity factor, k_1 , which is plotted in Figure 4.7 for comparison

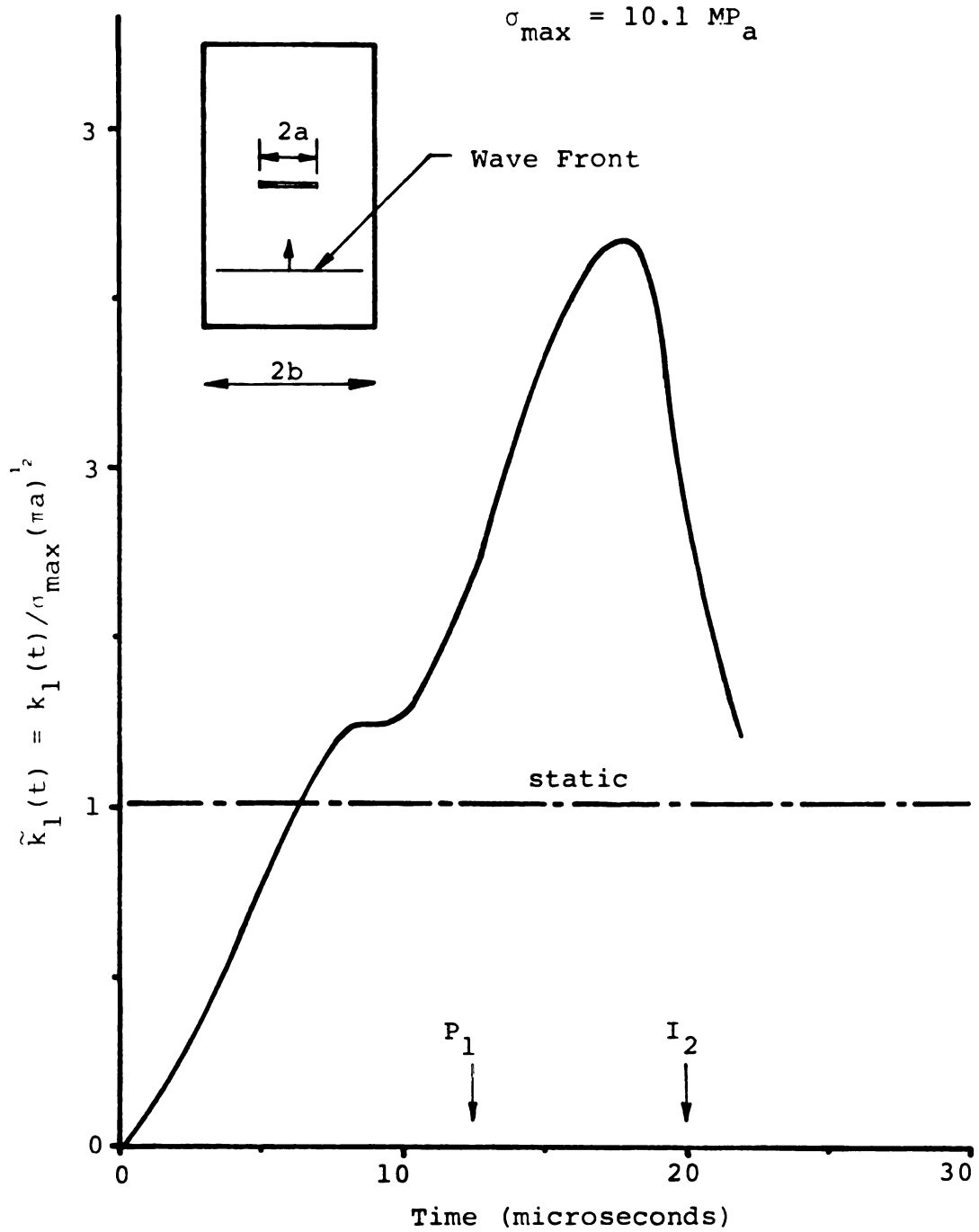


Figure 4.7. Variation of dynamic stress intensity factor with time for specimen with $a/b = 0.167$.

purposes, is computed using the formula in Reference [68]

$$\tilde{k}_1 = \frac{k_1}{\sigma(\pi a)} = F(a/b)$$

$$\tilde{k}_1 = [1 - 0.025 (a/b)^2 + 0.06 (a/b)^4] \sqrt{\sec \frac{\pi a}{2b}}$$

where,

a - half crack length

b - half the width of the specimen

As mentioned earlier, Thau and Lu [16] have shown that the mode I dynamic stress intensity factor for a Heaviside step loading of a finite crack in an infinite solid is 30% greater than the analogous static value. They also establish that this phenomena is due to the scattered Rayleigh waves. During the time period when the scattered waves from the boundary surfaces have not arrived, the initial response of a finite crack with neighboring boundaries should be identical to the response of a finite crack in an infinite plate subjected to an identical loading. Thus, if the specimen is such that the nearest boundary to the crack tip is sufficiently larger than the crack length the initial peak of the curve would represent the maximum response of a crack in an infinite plate. The experimental results give a dynamic overshoot of $k_1(t)$ of 27% in contrast to 35% obtained by Chen [19] for a Heaviside step loading of a bar having properties equivalent to that of steel.

Figure 4.8 shows the $\tilde{k}_1(t)$ -vs- t curve for a specimen with dimensions $2a = 1.25$ cm, $2b = 2.34$ cm and experimental data shown in Figure 3.3.

The crack profile for several time steps is shown in Figure 4.9. In this figure the normalized vertical displacement, $\eta/\bar{\eta}_0$, is plotted vs. the normalized distance, x/a , from the crack tip. The normalized static displacement at the center of the crack is computed using the formula in Reference [72] which is

$$\bar{\eta}_0 = \frac{2a}{E} [-0.071 - 0.535 (a/b) + 0.169 (a/b)^2 + 0.020 (a/b)^3 - 1.071 \frac{1}{(a/b)} \ln (1 - a/b)]$$

where,

$$\eta = U_y(t)/\sigma_{\max.}$$

$$\bar{\eta}_0 = U_y(t)/\sigma_{\max.} \quad \text{at the center of the crack}$$

The determination of k_1 as a function of crack length for a particular geometry is referred to as k -calibration. In recent years many geometries have been thoroughly studied by experimental, analytical and numerical means, for elastostatic loading conditions. The present investigation can give an estimate of the trend of the k -calibration for the elastodynamic loading condition, although such an estimate strictly applies only for identical loading. The experimental data for $k_1(t)_{\max}/\sigma_{\max}(\pi a)^{\frac{1}{2}}$ for two geometries as compared to

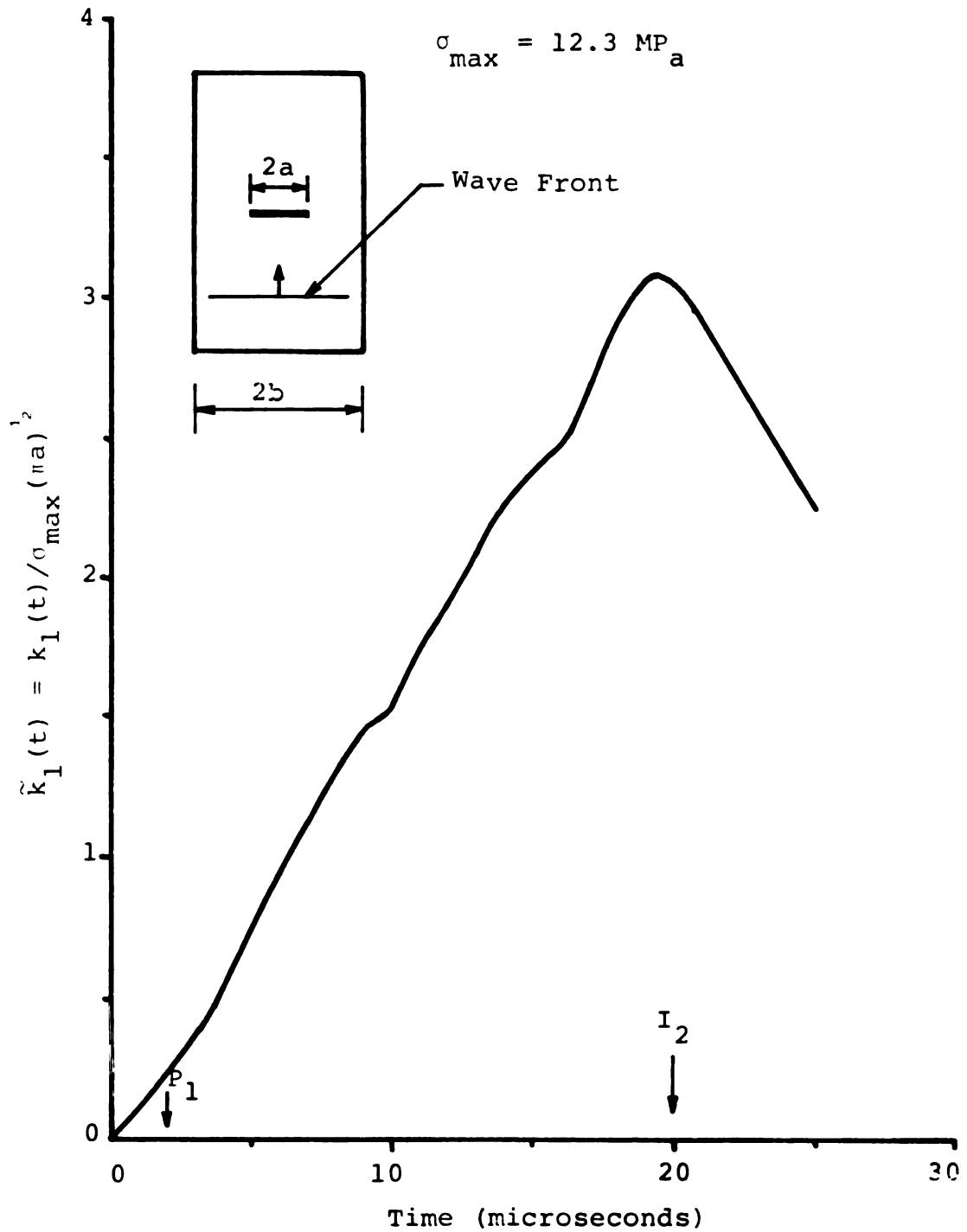


Figure 4.8. Variations of dynamic stress intensity factor with time for specimen with $a/b = 0.54$.

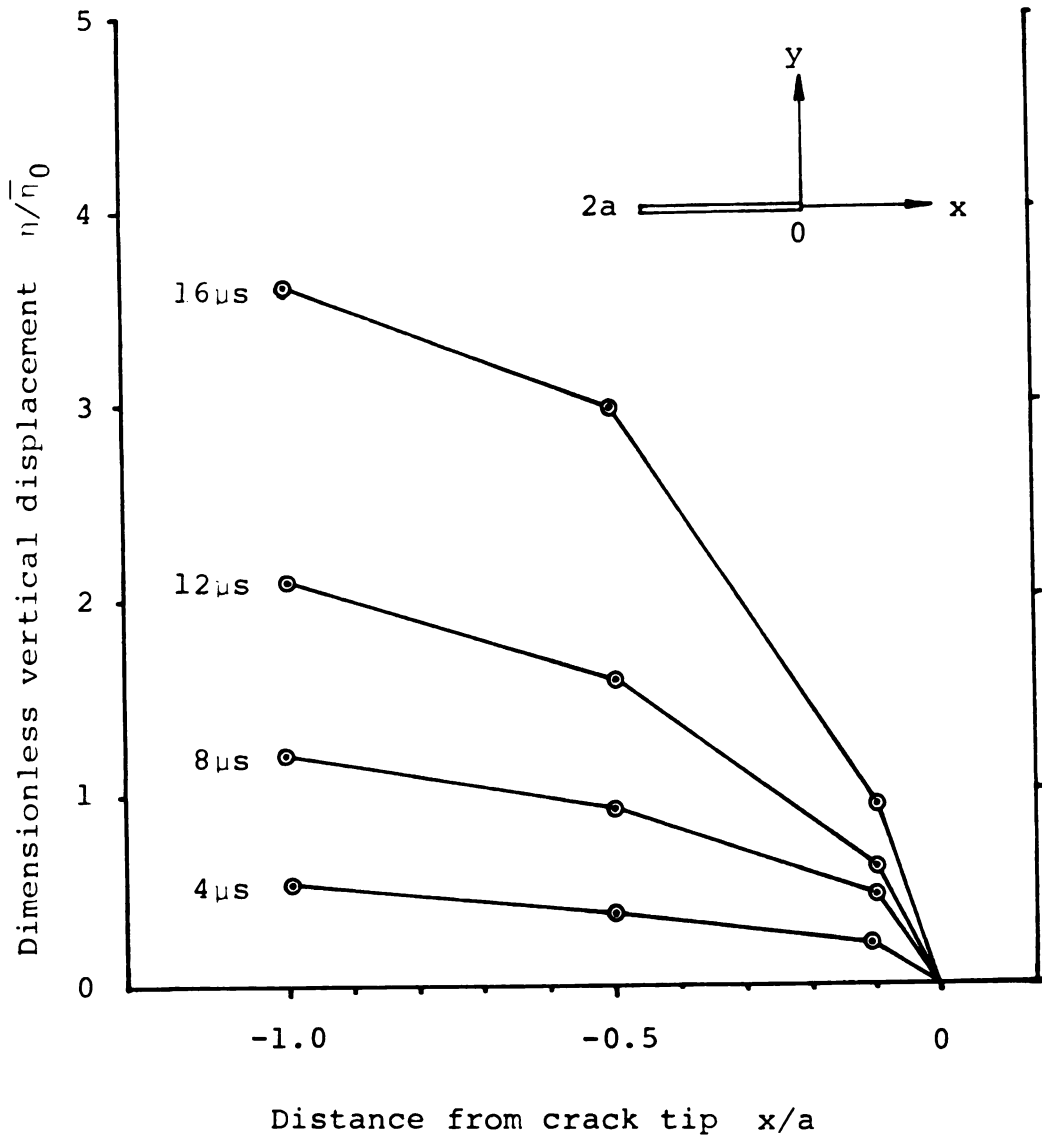


Figure 4.9. Crack profile at three different time steps.

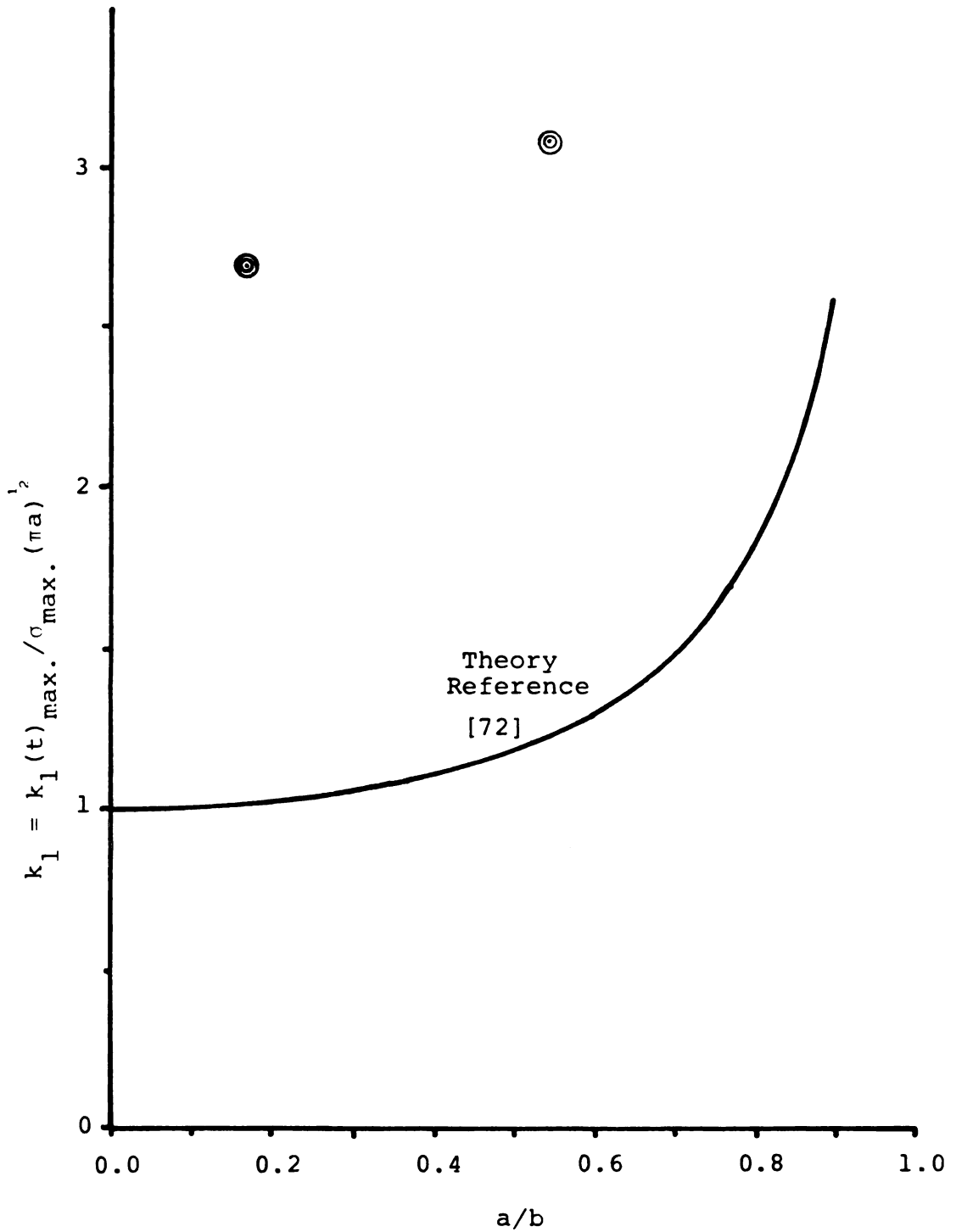


Figure 4.10. Comparison of experimental dynamic k-calibration data with theoretical static results.

theoretical k -calibration for the elastostatic case is shown in Figure 4.10. The comparatively long rise time for the narrow specimen is likely to influence the magnitude of $k_1(t)_{\max.}$.

4.3 CORRELATION WITH ANALYSIS

The normalized mode I stress intensity factor, $\tilde{k}_1(t)$, for various times after the arrival of the wave front at the crack, was determined using Equation 3.21. It should be noted that in Equation 3.21, $f(0) = 0$, therefore

$$\tilde{k}_1(t) = \int_0^t \frac{\partial f(t')}{\partial t'} {}_s\tilde{k}_1(t - t') dt'$$

In evaluating the foregoing integral, the experimental input pulse at location 2 was approximated by a ramp function time-varying force with a rise-time $t_R = 4.2$ microseconds as shown in Figure 4.11. The step response, ${}_s k_1(t)$, in Reference [16] was approximated by a ninth-order polynomial (least square fit). Also used in the evaluation was $C_p = 200,000$ in./sec., which was obtained from the experiment. The appropriate integration was then carried out by a simple numerical technique.

The result of the comparison is shown in Figure 4.12. The experimental result here represents the response during the time interval before the arrival of the reflected scattered waves from the nearest boundary.

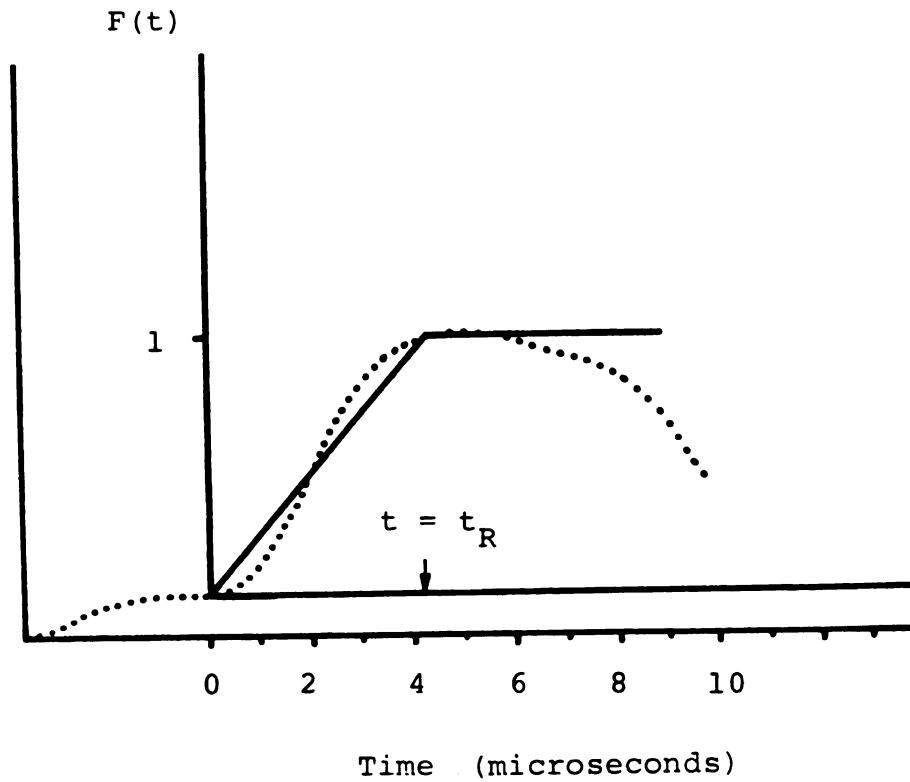


Figure 4.11. Input pulse at location 2; experimental points and ramp function approximation.

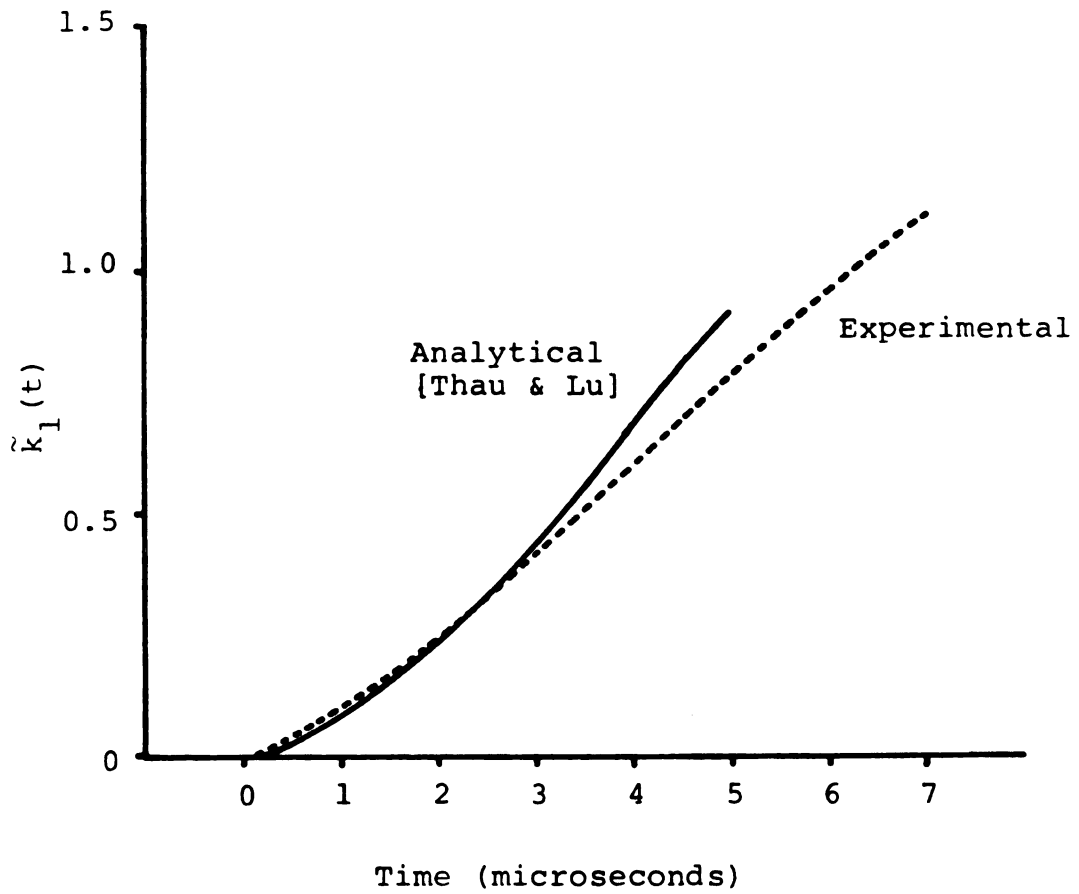


Figure 4.12. Comparison of analytical and experimental results for the dimensionless mode I stress intensity factor.

Also note that the theoretical result is shifted to omit the premature experimental response due to disturbance leading the pulse front.

As can be seen from Figure 4.12 the analytical result based on the work of Thau and Lu appear to do a good job of predicting the quantitative behavior of the experimental result. The deviations may be attributed to a number of reasons:

1. The ramp function pulse used in the analytical computation is an approximation of the actual pulse.
2. The states of stress and deformation are not truly two dimensional as assumed in the analytical computations.
3. The existence of a slight curvature to the wave front might add to the discrepancy.
4. Errors may have arisen in the digitizing and curve-fitting process.

4.4 COMPARISON WITH FINITE ELEMENT

King et al. [20], have reported finite element analyses of similar elastodynamic crack problems. Their analysis was carried out using a singularity element capable of mixed mode deformation and by simulating the incident wave by applying a step function time varying finite element equivalent of uniform stress at one end of the finite element model.

Professors King, Anderson, and Shreeves of Georgia Tech provided an analysis of this experiment. The finite element model they used is depicted in Figure 4.13. The model is a uniform grid model composed of 127 nodes, 200 ramp function time varying strain triangles, and one eight-node crack tip singularity-element. Constraints against horizontal displacement on the left edge of the model are dictated by symmetry of the problem with respect to a vertical axis through the center of the crack. A plane wave is induced by uniform loading on the upper edge of the model. In an effort to represent the behavior of the experimental model, the dimensions and the material properties for the finite element model were selected to correspond to that of the experimental model. The experimental pulse was approximated by a ramp function time varying force with a rise-time of five microseconds. The details of the finite element analysis may be found in Reference [20].

Figures 4.14 and 4.15 show comparisons of the finite element approximation with experimental results for the normalized mode I stress intensity factor and the normalized crack displacement at the center respectively. The finite element approximation and the experimental results show fairly good agreement for the short time results. It must be noted here that the short time experimental results have been corrected for the influence of the disturbance leading the wave front.

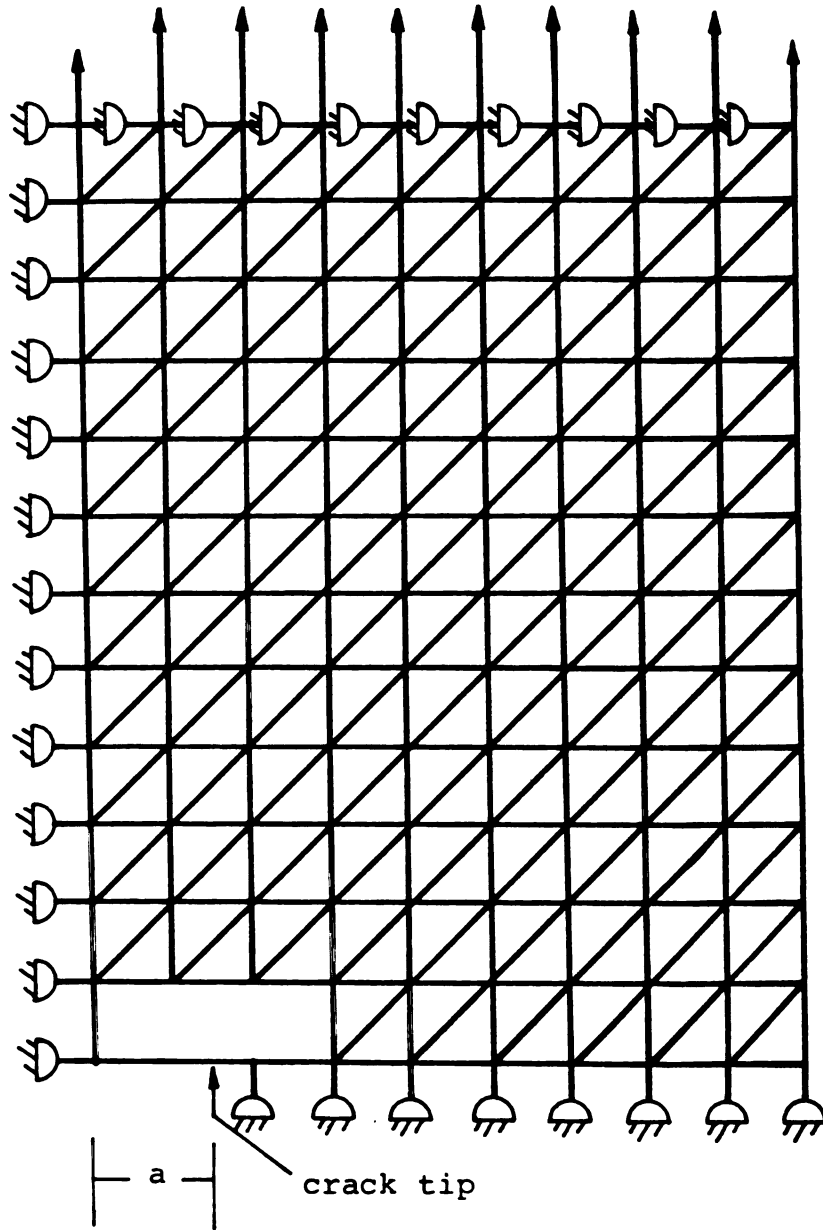


Figure 4.13. Finite element model.

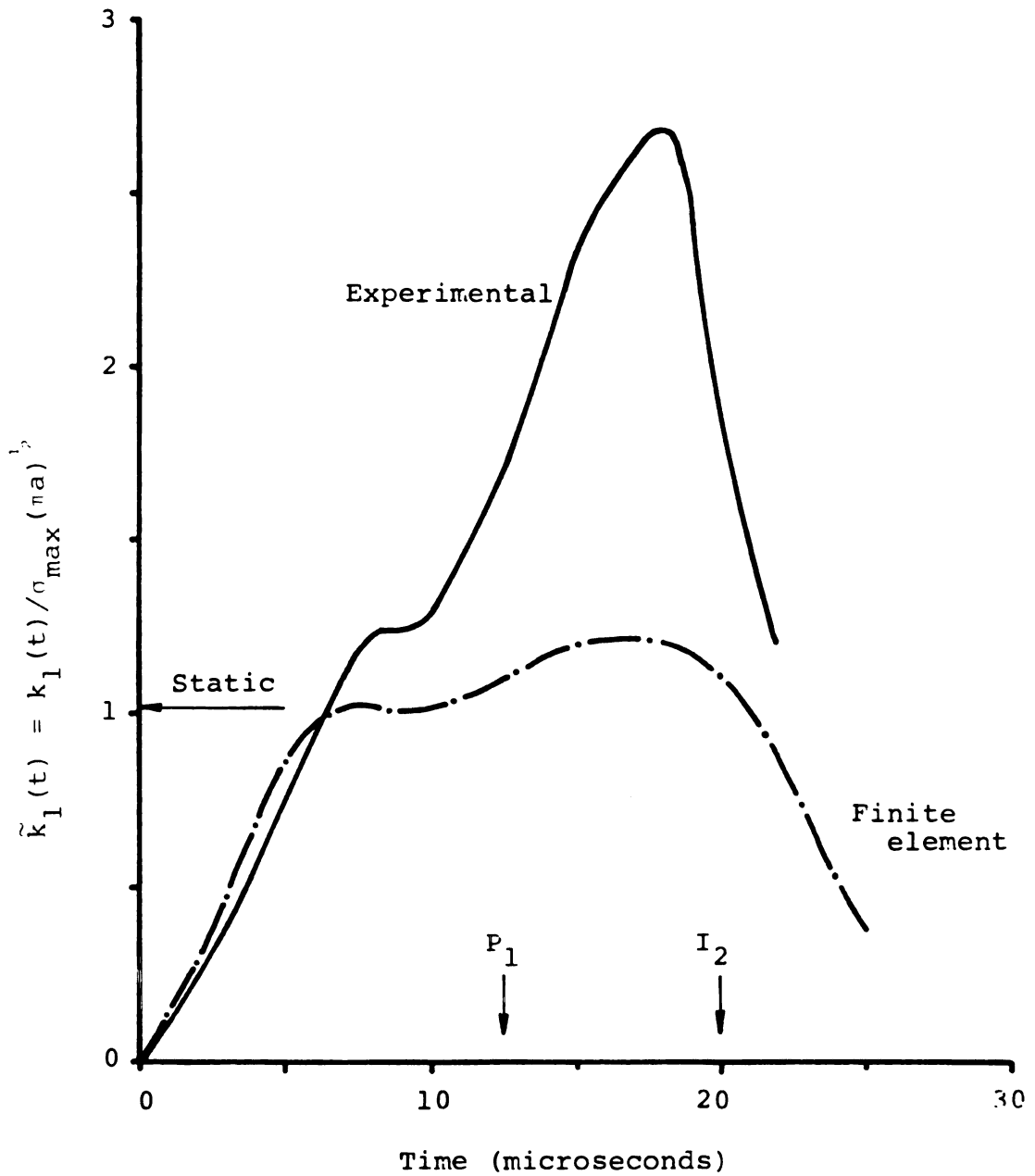


Figure 4.14. Comparison of finite element and experimental results for the dimensionless mode I stress intensity factor.

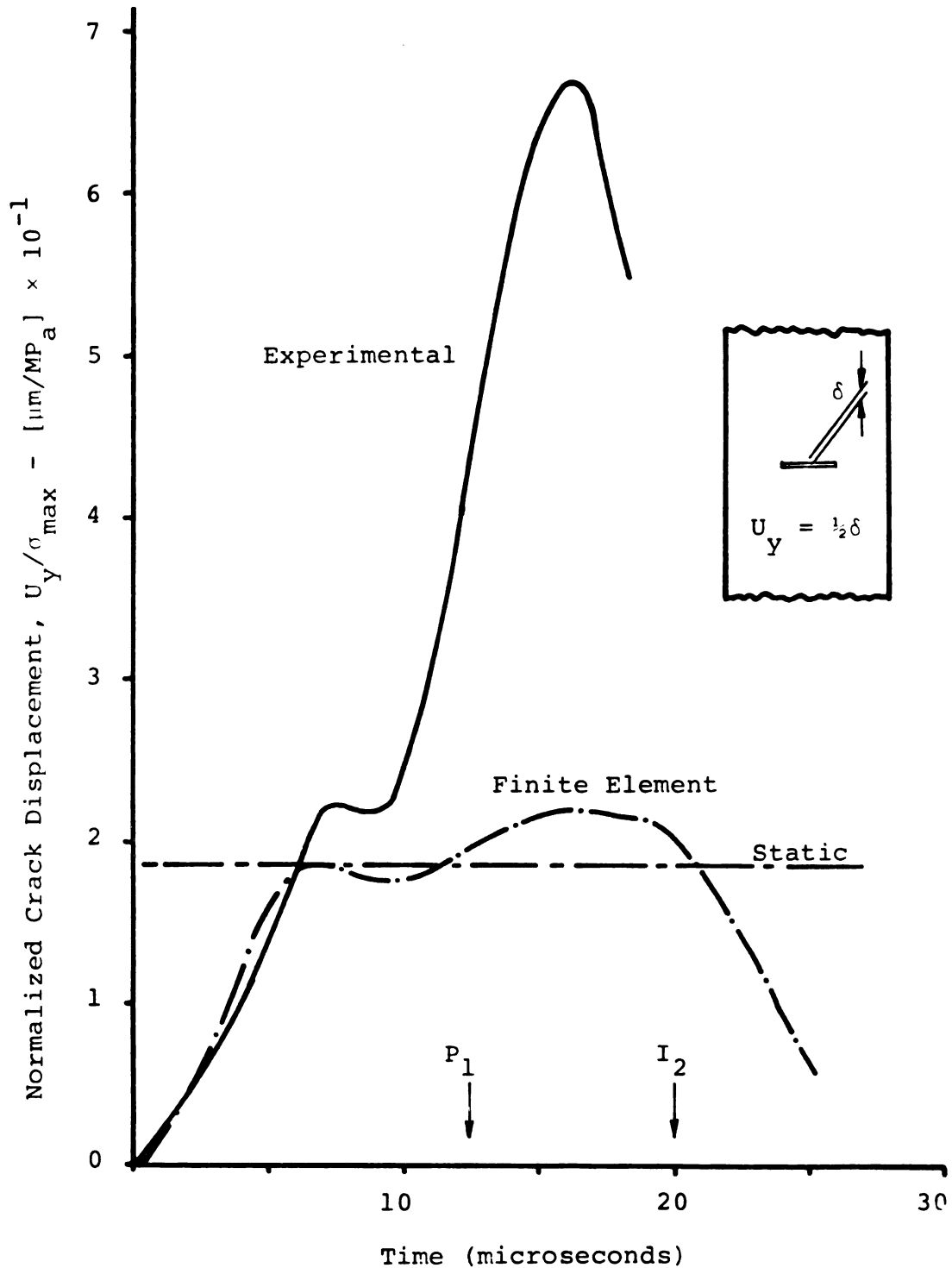


Figure 4.15. Comparison of finite element and experimental results for the normalized displacement at the center.

Although the qualitative behavior of the long time results seem to be similar, as evidenced by the curve shapes in Figures 4.14 and 4.15, the experimental results are not strictly comparable. The long-time experimental response is the sum effect of the "ramp" forcing function and the reflection from the lateral boundaries of the diffracted waves resulting from the impingement on the crack of the disturbance leading the wave front. This somewhat exaggerates the quantitative values of the long time experimental results. Also causing quantitative deviations may be the following reasons:

1. The ramp function time varying force used in the numerical computations is an approximation of the actual pulse.
2. The existence of a slight curvature to the wave front might add to the discrepancy.

Even though the quantitative values of the experimental curves may be somewhat exaggerated for reasons mentioned above, the finite element approximations are felt to under estimate the maximum stress intensity factor.

CHAPTER V

SUMMARY AND CONCLUSIONS

An apparatus that generates a plane tensile pulse in a plate with finite dimensions was developed. The pulse had an approximate shape of a ramp function with a rise-time of about five micro-seconds and a undisturbed flat top of about 30 micro-seconds. This loading apparatus was used in conjunction with the interferometric displacement gage (IDG) technique to study the dynamic response of a central crack in a finite plate subjected to longitudinal waves. The experiments were conducted for two different widths of the specimens. Three different sites along the faces of the crack were used to measure the displacements. Displacement-time curves were plotted for each site and points were taken from these curves to plot the crack profile for various time steps. Furthermore, the displacement-time result for the crack tip was used to compute the mode I dynamic stress intensity factor, $k_1(t)$.

The tensile impact apparatus generated a main pulse, which approximates a ramp function, and a precursor pulse. The precursor pulse may have been caused by imperfections of the impacting interfaces. The amplitude and

rise-time of the main pulse were fairly repeatable. Considering the difficulty of constructing such an apparatus, the financial and facility constraints at the time, the loading mechanism has proven to be satisfactory for the present investigation. Furthermore, the new apparatus has advantages over other techniques due to its simplicity, versatility, safety and low cost.

The interferometric displacement gage technique was successfully used in measuring dynamic crack displacements. Besides being easy to use the technique also proved to have the following definite advantages: satisfactory resolution, ease of specimen preparation and convenience of data recording.

The displacement-time and the normalized mode I dynamic stress intensity factor, $\tilde{k}_1(t)$, curves were found to oscillate, a phenomena attributed to the cancellation and reinforcement of the incident waves by various scattered waves. It was also found that the dynamic overshoot of $\tilde{k}_1(t)$ is 170% in contrast to Chen's numerical solution of 175% which corresponds to a Heaviside step function loading of a bar with Poisson's ratio of 0.3 and $a/b = 0.24$.

The analytical computations of $k_1(t)$, were carried out by employing the elastodynamic counterpart of the theory of generalized plane stress and the principle of superposition in time. The experimental results show good

agreement with analytical computations based on the results of Thau and Lu.

The finite element solutions provided by King et al. [73] compare favorably with the short time experimental results, i.e., with results for a time regime corresponding to the time it takes for the first scattered longitudinal wave to travel from a crack tip to the nearest boundary and back. The comparison of the long time results is not good. The discrepancy may be attributed to: the imperfect experimental wave front the influence of which could not be isolated for this time regime, and some ambiguity in fringe interpretation.

The dynamic stress intensity factor, in general, depends on the shape of the pulse, the wave length of the pulse, the crack length, the specimen geometry, and the Poisson's ratio of the material. In the present study emphasis was put on a particular ramp function type of pulse and a particular rectangular geometry of specimen. The development of an experimental technique for generating pulses of varying pulse shapes appears to be very desirable. Studies of the diffraction of a plane pulse by multiple normal cracks, by a single oblique crack, or by a combination of oblique and normal cracks appear to be a fruitful area for future investigators.

LIST OF REFERENCES

LIST OF REFERENCES

1. Griffith, A.A., "The Phenomena of Rupture and Flow in Solids", Phil. Trans. Roy. Soc. Lond. A221, 1920, pp. 163-194.
2. Erdogan, F., "Crack Propagation Theories", Fracture, Vol. 2, H. Liebowitz (ed.), Academic Press, New York, 1968, pp. 498-586.
3. Achenbach, J.D., "Wave Propagation, Elastodynamic Stress Singularities, and Fracture", Theoretical and Applied Mechanics, (W.T. Koiter, ed.) North Holland, Amsterdam, 1976, p. 71.
4. Achenbach, J.D., "Dynamic Effects in Brittle Fracture", Mechanics Today, (S. Nemat-Nasser, ed.), Pergamon, New York, 1972, p. 1.
5. Sih, G.C., "Some Elastodynamic Problems of Cracks", Int. J. Fracture Mech., 4, 1968, pp. 51-68.
6. Freund, L.B., "The Analysis of Elastodynamic Crack Tip Stress Fields", Mechanics Today, (S. Nemat-Nasser, ed.), Pergamon, New York.
7. Sih, G.C., and Loeber, J.F., "Wave Propagation in an Elastic Solid with a Line of Discontinuity or Finite Crack", Quarterly of Applied Mathematics, Vol. 27, 1969, pp. 193-213.
8. de Hoop, A.G., Representation Theorems for the Displacement in an Elastic Solid and Their Application to Elastodynamic Diffraction Theory, Doctoral Dissertation, Technische Hogeschool, Delft, 1958.
9. Nuismer, R.J., Jr., and Achenbach, J.P., "Dynamically Induced Fracture", J. Mech. Phys. Solids, Vol. 20, 1972, pp. 203-222.
10. Maue, A.W., "Die Entspannungswelle bei plötzlichem Eingeschnitt eines gespannten elastischen Körpers", Z. angew. Math. Mech., 34, 1954, pp. 1-12.

11. Ang, D.D., "Some Radiation Problems in Elastodynamics", Dissertation, Calif. Inst. Tech., Pasadena, Calif., 1958.
12. Baker, B.R., "Dynamic Stresses Created by a Moving Crack", J. Appl. Mech., 29, 1962, pp. 449-458.
13. Broberg, K.B., "The Propagation of a Brittle Crack", Arkiv for Fysik, 18, 1960, pp. 159-192.
14. Freund, L.B., "Crack Propagation in an Elastic Solid Subjected to General Loading -- I. Constant Rate of Extension", J. Mech. Phys. Solids, Vol. 20, 1972, pp. 129-140.
15. Papadopoulos, M., "Diffusion of Plane Elastic Waves by a Crack, with Application to a Problem of Brittle Fracture", J. Australian Math. Soc., 3, 1963, pp. 325-339.
16. Thau, S.A., and Lu, T.H., "Transient Stress Intensity Factors for a Finite Crack in an Elastic Solid Caused by a Dilatational Wave", Int. J. Solids Structures, 7, 1971, p. 731.
17. Sih, G.C., Embley, G.T., and Ravera, R.S., "Impact Response of a Finite Crack in Plane Extension", Int. J. Solids Structures, 8, 1972, pp. 977-993.
18. Chen, E.P., and Sih, G.C., "Transient Response of Cracks to Impact Loads", Mechanics of Fracture 4, Elastodynamic Crack Problems, G.C. Sih (ed.), Noordhoff, Leydon, 1977, pp. 1-57.
19. Chen, Y.M., "Numerical Computation of Dynamic Stress Intensity Factors by a Lagrangian Finite-Difference Method (The Hemp Code)", Eng. Fracture Mech., 7, 1975, p. 653.
20. Anderson, J.M., Aberson, J.A., and King, W.W., "Finite Element Analysis of Cracked Structures subjected to Shock Loads", Computational Fracture Mechanics, E.F. Rybicki, ed., ASME, New York, 1975.
21. Glazik, J.L., Jr., Numerical Analysis of Elastodynamic Near-Tip Stress Fields for Stationary and Propagating Cracks, Ph.D. Dissertation, Northwestern University, Evanston, Ill., 1976.

22. Aoki, S., Kishimoto, K., Kondo, H., and Sakata, M., "Elastodynamic Analysis of Crack by Finite Element Method Using Singular Element," Int. Journ. of Fracture, 14, 1978, pp. 59-68.
23. Hopkinson, J., "On the Rupture of Iron Wire by a Blow", Original Papers by the Late John Hopkinson II, B. Hopkinson (ed.), Cambridge University Press, Cambridge, 1901, pp. 316-320.
24. Hopkinson, B., "The Effects of the Detonation of Guncotton", Scientific Papers, Cambridge Univ. Press, Cambridge, 1921.
25. Rinehart, J.S., and Pearson, J., "Behavior of Metals under Impulsive Loads", Amer. Soc. for Metals, 1954.
26. Kolsky, H., and Rader, D., "Stress Waves and Fracture", Fracture, Vol. 1, H. Liebowitz (ed.), Academic Press, New York, 1969, pp. 553-569.
27. Roberts, D.K., and Wells, A.A., "The Velocity of Brittle Fracture", Engineering, 1954, pp. 820-822.
28. Schardin, H., "Velocity Effects in Fracture", Fracture, B.L. Averbach, D.K. Felbeck, G.T. Hahn, and D.A. Thomas (ed.), John Wiley & Sons, New York, 1959.
29. Clark, A.B.J., and Irwin, G.R., "Crack Propagation Behaviors", Exp. Mech., 6, 1966, pp. 321-330.
30. Kolsky, H., "The Stress Pulses Propagated as a Result of the Rapid Growth of Brittle Fracture", Eng. Fracture Mech., 5, 1973, pp. 513-522.
31. Wells, A.A., and Post, D., "The Dynamic Stress Distribution Surrounding a Running Crack -- a Photoelastic Analysis", Proc. SESA, 16, 1958, pp. 69-92.
32. Pratt, P.L., and Stock, T.A.C., "The Distribution of Strain about a Running Crack", Proc. Roy. Soc. Lond., A285, 1964, pp. 73-82.
33. Kobayashi, A.S., Bradley, W.B., and Selby, R.A., "Transient Analysis in a Fracturing Epoxy Plate with a Central Crack", Proc. Int. Conf. on Fracture, Sendai, Japan, 1965.
34. Bradley, W.B., and Kobayashi, A.S., "An Investigation of Propagating Cracks by Dynamic Photoelasticity", Exp. Mech., 10, 1970, pp. 106-113.

35. Sommer, E., and Soltesz, U., "Crack-Opening-Displacement Measurements of a Dynamically Loaded Crack", Eng. Fracture Mech., 2, 1971, pp. 235-241.
36. Smith, C.C., and Knauss, W.G., "Experiments on Critical Stress Intensity Factors Resulting from Stress Wave Loading", Mech. Res. Comm., 2, 1975, pp. 187-192.
37. Costin, L.S., Duffy, J., and Freund, L.B., "Fracture Initiation in Metals Under Stress Wave Loading Conditions", Fast Fracture and Crack Arrest, ASTM STP627, G.T. Hahn and M.F. Kanninen (eds.), Amer. Soc. Test. Mater., 1977, pp. 301-318.
38. Theocaris, P.S., and Katsmanis, F., "Response of Cracks to Impact by Caustics", Eng. Fracture Mech., 10, 1978, pp. 197-210.
39. Mason, W., "The Yield of Steel Wire Under Stresses of Very Small Duration", Proc. Instn. Mech. Eng., Lond., Vol. 128, 1934, p. 409.
40. Ginns, D.W., "The Mechanical Properties of Some Metals and Alloys Broken at Ultra High Speeds", J. Inst. Met., Vol. 61, 1937, p. 61.
41. Brown, A.F.C., and Vincent, N.D.G., "The Relation between Stress and Strain in the Tensile Impact Test", Proc. Instn. Mech. Engrs. Lond., Vol. 145, 1941, p. 126.
42. Clark, D.S., "The Influence of Impact Velocity on the Tensile Characteristics of Some Aircraft Metals and Alloys", N.A.C.A. Technical Note No. 868, 1942.
43. Mann, H.C., "High-Velocity Tension -- Impact Tests", Proc. Amer. Soc. Test. Mater., Vol. 36, Part 2, 1936, p. 85.
44. Nadai, A. and Manjoine, M.J., "High-Speed Tension Tests at Elevated Temperatures", J. Appl. Mech., Vol. 8, 1941, p. A-77.
45. Clark, D.S. and Wood, D.S., "The Time Delay for the Initiation of Plastic Deformation at Rapidly Applied Constant Stress", Proc. Amer. Soc. Test. Mater., Vol. 49, 1949, p. 717.
46. Austin, A.L. and Steidel, R.F., Jr., "A Method for Determining the Tensile Properties of Metals at High Rates of Strain", Proc. Soc. Exp. Stress Anal., Vol. 17, 1959, pp. 99-114.

47. Hunt, D. Le M., "Very High Speed Yield of Mild Steel in Tension", N.C.R.E. Report No. R427A, 1961.
48. Harding, J., Wood, E.O., and Campbell, J.D., "Tensile Testing of Materials at Impact Rates of Strain", J. Mech. Engr. Sci., Vol. 2, No. 2, 1960, pp. 88-96.
49. Harding, J., "Tensile Impact Testing by a Magnetic Loading Technique", J. Mech. Engr. Sci., Vol. 7, No. 2, 1965, pp. 163-176.
50. Jenkins, F.A., and White, H.E., "Fundamentals of Optics", McGraw-Hill, New York, 1957.
51. Sharpe, W.N., Jr., "Interferometric Surface Strain Measurement", Int. J. of Nondestructive Test., Vol. 3, 1971, pp. 56-76.
52. Sharpe, W.N., Jr., "Dynamic Strain Measurement with the Interferometric Strain Gage", Exp. Mech., Vol. 10, 1970, pp. 89-92.
53. Paris, P.C., and Sih, G.C., "Stress Analysis of Cracks", Fracture Toughness Testing and Its Applications, ASTM STP381, Amer. Soc. Test. Mater., 1965, pp. 30-81.
54. Adams, N.J.I., "Fatigue Crack Closure at Positive Stresses", Eng. Fracture Mech., Vol. 4, 1971, pp. 593-595.
55. Elber, W., "The Significance of Fatigue Crack Closure", Damage Tolerance in Aircraft Structures, ASTM STP 486.
56. Dudderar, T.D., and Gorman, H.J., "The Determination of Mode I Stress-Intensity Factors by Holographic Interferometry", Exp. Mech., Vol. 13, No. 4, 1973, pp. 145-149.
57. Sommer, E., "An Optical Method for Determining the Crack-Tip Stress Intensity Factor", Eng. Fracture Mech., Vol. 1, 1970, pp. 705-718.
58. Crosely, P.B., Mostovoy, S., and Ripling, E.J., "An Optical-Interference Method for Experimental Stress Analysis of Cracked Structures", Eng. Fracture Mech., Vol. 3, 1971, pp. 421-433.

59. Evans, W.T., and Luxmore, A., "Measurement of In-Plane Displacements Around Crack Tips by a Laser Speckle Method", Eng. Fracture Mech., Vol. 6, 1974, pp. 735-743.
60. Sharpe, W.N., Jr., and Grandt, A.F., Jr., "A Laser Interferometric Technique for Crack Surface Displacement Measurements", Proc. 20th Int. Instr. Symp. Instr. Soc. Amer., Albuquerque, N.M., 1974.
61. Sharpe, W.H., Jr., and Grandt, A.F., Jr., "A Preliminary Study of Fatigue Crack Retardation Using Laser Interferometry to Measure Crack Surface Displacements", ASTM STP 601, Amer. Soc. Test. Mater., 1976, pp. 302-320.
62. Macha, D.E., Sharpe, W.N., Jr., and Grandt, A.F., Jr., "A Laser Interferometric Method for Experimental Stress Intensity Factor Calibration", ASTM STP 601, Amer. Soc. Test. Mater., 1976, pp. 490-505.
63. Sharpe, W.N., Jr., "A New Biaxial Strain Gage", Review of Scientific Instruments, Vol. 41, No. 10, 1970, pp. 1440-1443.
64. Altiero, N.J., and Sharpe, W.N., Jr., "Measurements of Mixed-Mode Crack Surface Displacements and Comparison with Theory", Final Report on NASA grant NSG-3101, 1978.
65. Kobayashi, A.S., "Experimental Techniques in Fracture Mechanics", Iowa State Univ. Press, Ames, Iowa, 1973.
66. Ranganath, S., "An Improved Method of Triggering Oscilloscopes for Dynamic-strain Measurements", Exp. Mech., Vol. 13, 1973, pp. 397-400.
67. Davies, R.M., "A Critical Study of the Hopkinson Pressure Bar", Phil Trans. Roy. Soc. Lond., Ser. A, Vol. 240, 1948, pp. 375-457.
68. Mindlin, R.D., "An Introduction to the Mathematical Theory of Vibrations of Elastic Plates", U.S. Army Signal Corps Eng. Laboratory, Fort Monmouth, N.J., 1955.
69. Dally, J.W., Riley, W.F., and Durelli, A.J., "A Photoelastic Approach to Transient Stress Problems Employing Low-Modulus Materials", J. Appl. Mech., Vol. 26, Trans. ASME, Vol. 81, Series E, 1959, pp. 613-620.

70. Durelli, A.J., and Riley, W.F., "Research Studies of Stress Waves in Earth and Model Earth Media", AFSWC Tech. Report 60-4, Contract AF 29(601)1167, Project 1080, Task 10801, Armour Research Foundation, 1959, pp. 96-116.
71. Feder, J.C., Gibbons, R.A., Gilbert, J.T., and Offenbacher, E.L., "The Study of the Propagation of Stress Waves by Photoelasticity", Proc. Soc. Exp. Stress Anal., 14, 1956, pp. 109-117.
72. Tada, H., Paris, P., and Irwin, G., "The Stress Analysis of Cracks Handbook," Del Research Corporation, Hellertown, Pa., 1973.
73. King, W.W., Anderson, J.M., and Shreeves, personal communication.

MICHIGAN STATE UNIVERSITY LIBRARIES



3 1293 03146 1803